The Astrophysical Journal, 678:922–938, 2008 May 10

TIDAL INTERACTIONS OF RED GIANTS WITH ENVIRONMENT STARS IN GLOBULAR CLUSTERS

Shimako Yamada,[1] Atsuo T. Okazaki,[2] and Masayuki Y. Fujimoto[1]

Received 2007 September 6; accepted 2008 January 13

ABSTRACT

We investigate the tidal interactions of a red giant with a main-sequence star in the dense stellar core of globular clusters by the smoothed particle hydrodynamics method. Two models of 0.8 $M_\odot$ red giants with surface radii 20 and 85 $R_\odot$ are used with a 0.6 or 0.8 $M_\odot$ main-sequence star treated as a point mass. We demonstrate that even for the wide encounters in which the two stars fly apart, the angular momentum of orbital motion can be deposited into the red giant envelope to such an extent as to trigger rotational mixing and to explain the fast rotation observed for the horizontal branch stars, and also that sufficient mass can be accreted on the main-sequence stars to disguise their surface convective zone with the matter from the red giant envelope. On the basis of the present results, we discuss the parameter dependence of these transfer characteristics with nonlinear effects taken into account and derive fitting formulae to give the amounts of energy and angular momentum deposited into the red giant and of mass accreted onto the perturber as functions of the stellar parameters and the impact parameter of the encounter. These formulae are applicable to the encounters not only of the red giants but also of the main-sequence stars and are useful in the study of the evolution of stellar systems with the star-star interactions taken into account.

Subject headings: accretion, accretion disks — hydrodynamics — methods: numerical — stars: horizontal-branch — stars: Population II

Online material: color figures

1. INTRODUCTION

In the core of globular clusters, it is thought that star-star interactions play an important role because of very high stellar density and relatively low velocity (Hills & Day 1976). There is growing evidence for the modifications of stellar properties and populations under the influence of close encounters and collisions. For example, the overabundance of low-mass X-ray binaries and millisecond pulsars is regarded as consequent on tidal captures of an environment star by neutron stars and on the exchange encounters involving a neutron star (Fabian et al. 1975; Hills 1976); the smaller relative frequency of red giants in the core is attributed to the deprival of their envelope during close encounters with environment stars (Djorgoski et al. 1991; Beer & Davies 2004). Blue stragglers, which are main-sequence stars more massive than the turnoff stars, may result from a direct collisional coalescence and/or binary merge of two or more stars (Leonard 1989; see Mapelli et al. 2006; Leigh et al. 2007 and references therein for recent works); see also reviews by Bailyn (1995), Hut et al. (2003), and Ferraro (2006). In particular, the inflation of the number of known blue stragglers, boosted by the observations using the *Hubble Space Telescope* (Ferraro et al. 1997, 1999, 2003, 2004; Paltrinieri et al. 2001; Sabbi et al. 2004; Beccari et al. 2006; Warren et al. 2006), suggests that a significant fraction of stellar populations undergo such encounters with neighboring stars. Recent observations with *Chandra* indicate a link between the number of X-rays binaries and the stellar encounter rates in globular clusters (Pooley et al. 2003; Pooley & Hut 2006).

Furthermore, there is a long-standing problem of large star-to-star variations in the surface abundances of light elements such as C, N, O, Ne, Mg, and Al. Some giants in globular clusters exhibit the anomalous surface abundances that cannot be explained in terms of nucleosynthesis and material mixing in the stars within the current standard framework of stellar evolution (e.g., see reviews by Kraft 1994; Da Costa 1997). Since these anomalies are observed only in globular clusters but not from field giants in the Galactic halo, it is natural to search for their origin(s) in the differences between the environment in the globular clusters and in the Galactic halo and, hence, to consider them as evidence of the star-star interactions. In fact, Fujimoto et al. (1999) have proposed a scenario for the formation mechanism of these abundance anomalies involving hydrogen shell flashes in red giants, as a result of internal mixing, triggered by the deposition of angular momentum into their envelopes during a close encounter with other stars. It is demonstrated that this extramixing model can reproduce the observed relationship such as correlation and scatter in the anomalous abundances of Na and Al and the Mg-Al anticorrelation (Aikawa et al. 2001, 2004).

Recently, similar abundance variations have been found among unevolved turnoff and subgiant stars (Gratton et al. 2001). It is true that the variations and anticorrelations between CN and CH bands have been reported not only for giants but also for stars of the upper main sequence, which may be taken to suggest the presence of abundance anomalies in unevolved stars (Suntzeff & Smith 1991; Briley et al. 1992; Cannon et al. 1998; Cohen 1999). It has been argued that these facts refute the evolutionary scenario that the abundance anomalies are produced during the evolution along the giant branch and favor the primordial scenario that the stars were born of gas already subject to the anomalous abundances (e.g., Sneden et al. 2004). As a possible compromise, recycling scenarios have been proposed in which the inhomogeneity is due to the surface pollution from accreting the ejecta of anomalous abundances from the erstwhile asymptotic giant branch (AGB) stars of intermediate masses (Thoul et al. 2002) or in which the second-generation stars were born from the gas polluted with the ejecta of AGB stars (D'Antona 2004; D'Antona & Caloi 2004). Ventura et al. (2001) argue that the burning at the bottom of the convective zone in low-metallicity AGB stars can produce the observed O-Na and Mg-Al anticorrelations. On the other hand, Fenner et al. (2004) cast doubt on the relevance of AGB ejecta to

[1] Department of Physics, Hokkaido University, Kita-ku, Sapporo 060-0810, Japan.
[2] Faculty of Engineering, Hokkai-Gakuen University, Toyohira-ku, Sapporo 062-8605, Japan.

the observed anomalies. In addition, the scenarios involve serious difficulties both in the mass supply and in the overabundances of CN and *s*-process elements, attendant with the third dredge-up during the evolution; the amount of mass ejecta necessary to cover and disguise the surface convection of giants may well exceed the total envelope mass that can be ejected from the erstwhile AGB stars, and the enrichment of *s*-process elements is never observed (James et al. 2004).

For the evolutionary scenario, it can also be argued that the abundance anomalies are printed onto the surface of unevolved stars through the mass transfer during the close encounters with such giants that have already developed the abundance anomalies; the anomalous abundances are themselves attributed to the deposition of angular momentum into the convective envelope of giants during prior close encounters with environment stars (Shimada et al. 2003). The surface convection of Population II main-sequence stars contains masses of $3 \times 10^{-3}\ M_{\odot}$ near the turnoff (e.g., see Fujimoto et al. 1995), and hence, the accretion of mass of this order may suffice to disguise their surface abundances with those of accreted matter. The evolutionary scenario, with star-star interactions during the red giant branch (RGB) taken into account, is free from the above difficulties and has a fair prospect of giving a satisfactory explanation to these inhomogeneous anomalies. Recently, the helium production by this extramixing mechanism is discussed (Suda et al. 2007) in relation to the splitting of the main-sequence branch, observed from ω Cen (Bedin et al. 2004) and from NGC 2808 (Piotto et al. 2007).

One of the aims of this paper is to investigate whether the orbital angular momentum can be transferred into the envelope of a giant from the orbital motion and whether the main-sequence star can accrete the envelope mass from giants enough to disguise their surface layer with the accreted matter through star-star interactions. It is argued that the rotation-induced mixing requires (differential) rotation of $\sim$0.01 times the local critical rate from the energetic viewpoint (e.g., see Fujimoto et al. 1999), although the proper theory is yet to be established. From the observations, the horizontal branch (HB) stars are known to display a bimodal distribution of rotation velocity with the fastest rotators at velocity $v_{\rm rot} \sin i \gtrsim 30$ km s^{-1} (where i is the inclination angle of the spin axis) on the cooler side of the HB where $T_{\rm eff} < 15{,}000$ K (Peterson 1983; Peterson et al. 1995; Cohen & McCarthy 1997; Behr et al. 2000a, 2000b; Recio-Blanco et al. 2002). If we neglect the angular momentum loss during the transition to the HB, such rapid rotations require angular momentum corresponding to the rotation rate of the order of $\Omega \simeq 0.01\Omega_{\rm rg}$ at the tip of the RGB ($\Omega_{\rm rg}$ being the critical rotation rate at the surface). This poses a problem of the origin of angular momentum, since in the low-mass stars, the angular momentum is effectively extracted by magnetic braking during the main-sequence phase and by mass loss during the red giant phase (e.g., see Recio-Blanco et al. 2002; Suda & Fujimoto 2006).

The star-star interactions have been proposed as the mechanism(s) to form the unusual stellar objects discussed above and have been studied by many authors. Among the analytical approaches, Fabian et al. (1975) first presented an idea and evaluated the possibility that the low-mass X-ray binaries are produced through tidal dissipation during the two-body encounters involving a neutron star or low-mass black hole. Press & Teukolsky (1977) developed the linear perturbation theory of the two-body tidal capture mechanism to derive a general formula for the amount of orbital energy deposited into the oscillatory modes of the stellar envelope during a periastron passage. Lee & Ostriker (1986) and McMillan et al. (1987) worked out the cross sections for the binary formation via tidal capture of a main-sequence star and McMillan et al. (1990) worked out that of a red giant. These studies are, however, limited to the linear regime and cannot deal with the nonlinear effects such as the mass transfer between the stars and the mass loss from the stars owing to large deformations of the stars by tidal forces.

In order to estimate the nonlinear effects during the close encounters, numerical simulations are necessary. Among the numerical approaches, most studies have been devoted to understanding the resultant offspring of the stellar interactions. Simulations of tidal encounters have been performed for various combinations of stars, e.g., a main-sequence star and a red giant star (Benz & Hills 1991), a neutron star and a main-sequence star or a red giant star in an attempt to explain the formation of the low-mass X-ray binaries and the millisecond pulsars (Davies et al. 1992; Rasio & Shapiro 1991; Davies 1995; Lee et al. 1996), main-sequence stars in encounters and collisions, aiming at the formation of blue stragglers (Lai et al. 1993; Lombardi et al. 2002), and a red giant star and a neutron star in relation to the formation of pulsars or ultracompact X-ray binaries (Rasio & Shapiro 1991; Lombardi et al. 2006). These studies have been performed exclusively by using the smoothed particle hydrodynamics (SPH) method, except for the encounters involving a massive black hole and a star, which were calculated by using a three-dimensional Euler hydrodynamic code (Khokhlov et al. 1993a, 1993b). Recently, SPH simulations have been applied to the evolution of a giant planet through the tidal interactions with a Sun-like star (Faber et al. 2005; Ivanov & Papaloizou 2004).

The former hydrodynamic simulations, especially those of the tidal encounters between a red giant and a main-sequence star by Davies et al. (1991), have been carried out with a relatively small number of SPH particles and for a limited range of parameters. Their results are thought to be subject to limitations arising from low mass resolutions, since the mass involved in the interactions decreases as the periastron distance increases, and the SPH method may not give a valid description of such situations where mass scales are as small as that allotted to each particles. In our problems of surface pollution, we deal with the accretion of mass $\sim 10^{-3}\ M_{\odot}$. Simulations with finer mass resolutions, and hence with larger particle numbers, are necessary to investigate such encounters involving the transfer of mass of this order. It is also desirable to perform simulations for a wide range of parameters, such as the periastron distance, the red giant models in different evolutionary stages, and the mass of main-sequence stars, in order to obtain realistic and general information about the characteristics of the tidal interactions.

In this paper we first carry out simulations of tidal interactions between a red giant and a main-sequence star by using the SPH method. We make a detailed analysis of the amounts of energy and angular momentum transferred from the orbital motion to the oscillation and spin of the red giant and the amount of mass lost from the red giant and accreted onto the main-sequence stars. Based on the numerical experiments, we then attempt to clarify the parameter dependence of these characteristics and to formulate the quantitative outcome as simple functions of the stellar parameters and impact parameter of encounters. The present results are applied to investigate the relevance of the scenario in which the star-star interactions give rise to the abundance anomalies observed among not only giants but also main-sequence stars in globular clusters. The derived formulae will be useful for performing simulations of dynamical evolution of stellar systems with the effects of stellar interactions taken into account.

The organization of the paper is as follows. In § 2 we describe our numerical methods, including the setup of the initial conditions, the models of the red giant, the treatment of accretion,

and the determination of the viscosity of red giant models. In § 3 we present the results from our simulations with the discussion of the nonlinear effects of tidal interactions. In § 4 we derive fitting formulae for the energy and angular momentum deposited into the envelope of the red giants and the mass accreted onto the main-sequence stars during the tidal encounters. The conclusions follow in § 5, with the discussion about the application to the globular clusters.

2. METHOD OF NUMERICAL COMPUTATIONS

In the present work we use the three-dimensional, SPH code, originally developed by Benz (Benz 1990; Benz et al. 1990) and extended by Bate et al. (1997). The variable smoothing length is adopted with the hierarchical tree method, originally written by Press (1986) to make a list of the particles in the closest neighborhood of a particle. The kernel and the integrating method in our code are respectively the standard cubic spline kernel and a second-order Runge-Kutta-Fehlberg integrator with individual time steps for each particle (Bate et al. 1997).

In our cases, the timescale of periastron passing is much shorter than the Helmholtz-Kelvin timescale in the envelope [$\tau_{\rm HK} \simeq 1.5 \times 10^4 (R_{\rm rg}/20\ R_\odot)^{-1} (L_{\rm rg}/L_\odot)^{-1}$ yr, where $R_{\rm rg}$ is the surface radius of the red giant]. Accordingly, we assume the adiabatic relation for the gas in the envelope of red giants. In actuality, the code takes into account the change of the entropy due to viscous dissipation, although it may have only a minor effect, since we deal with the tidal interactions at large distances, not accompanied by large shock dissipation.

Our SPH code uses the standard form of artificial viscosity with two free parameters $\alpha_{\rm SPH}$ and $\beta_{\rm SPH}$, which respectively control the strength of the shear and bulk viscosity components and that of a second-order, von Neumann–Richtmyer-type viscosity (Monaghan & Gingold 1983). It is known that the linear artificial viscosity can be reduced to the Shakura-Sunyaev viscosity prescription in the continuous limit; Meglicki et al. (1993) derived a relation which connects the viscous force with the linear artificial viscous parameter $\alpha_{\rm SPH}$. If the density varies on a length scale much larger than the velocity, the shear viscosity, ν, is written in terms of the artificial viscosity parameter $\alpha_{\rm SPH}$, in the form

$$\nu = (1/10)\alpha_{\rm SPH} c_s h, \tag{1}$$

where c_s is the isothermal sound velocity and h is the smoothing length (Okazaki et al. 2002). In the envelope of red giants, on the other hand, we may relate the shear viscosity to the eddy viscosity of convective motions, $\nu_{\rm eddy}$, evaluated at

$$\nu_{\rm eddy} = v_{\rm conv} l_{\rm mix}. \tag{2}$$

where $v_{\rm conv}$ is the averaged velocity of convective elements and is estimated from the mixing length theory with the mixing length, $l_{\rm mix}$. For a red giant model of mass 0.8 $M_\odot$ and the metallicity $[{\rm Fe/H}] = -1.5$, the eddy viscosity is found to be nearly constant around $\nu_{\rm eddy} \simeq 7 \times 10^{15}$ cm^2 s^{-1} in the envelope when the radius $\sim$20 $R_\odot$ and the luminosity $\sim$100 $L_\odot$ (see, e.g., Suda & Fujimoto 2006). Since $c_s h \simeq 7 \times 10^{17}$ cm^2 s^{-1} on average for the red giant models constructed with SPH code (see below), we may approximate the eddy viscosity with a choice of $\alpha_{\rm SPH} = 0.1$. We perform the simulations with two values of the linear artificial viscosity parameter, $\alpha_{\rm SPH} = 1.0$, which is of common use, and $\alpha_{\rm SPH} = 0.1$ in order to see the effects of viscous forces. As for the nonlinear artificial viscosity parameter, we follow the usual prescription and set $\beta_{\rm SPH} = 2\alpha_{\rm SPH}$ (Bate et al. 1997).

2.1. *Initial Conditions and Approximations*

Our simulations consist of two steps, i.e., we first make the initial models of red giants in hydrostatic equilibrium with SPH particles and then follow the encounter with a main-sequence star. Our red giant models are constructed with a total of 50,000 SPH particles of equal mass in the envelope and the core approximated by an appropriate external potential, while the main-sequence star is treated as a point mass. We start the encounter simulations by placing a red giant and a main-sequence star at a separation of $5R_{\rm rg}$. Their relative velocity at this distance is calculated from the relative velocity at infinity, assumed to be $v_\infty = 10$ km s^{-1} in this work, and the impact parameter. The red giants are assumed to be not rotating initially. We set the total mass at $M_{\rm rg} = 0.8\ M_\odot$ and adopt two models at the different evolution stages, one with the core mass $M_{\rm core} = 0.32\ M_\odot$ and the surface radius $R_{\rm rg} = 20\ R_\odot$ and the other with $M_{\rm core} = 0.48\ M_\odot$ and $R_{\rm rg} = 85\ R_\odot$; the mass of one SPH particle is 0.96×10^{-5} and $0.64 \times 10^{-5}\ M_\odot$, respectively. The former model is taken to have the same model parameters as the model from Benz & Hills (1991) and Davies et al. (1991) who use 7132 SPH particles of unequal masses, and the latter corresponds to the structure realized near the tip of the RGB. For the main-sequence star, we take two different masses of $M_{\rm ms} = 0.6$ and $0.8\ M_\odot$.

2.2. *Red Giant Models*

The envelope structure of the red giant can be reproduced by placing the envelope mass under the influence of the gravity of the core, modeled as a sphere of uniform density, according to Fujimoto & Tomisaka (1992). By solving the equations of hydrostatic equilibrium with an additional gravity g of the core, expressed as

$$g = \begin{cases} -GM_{\rm core} r/R_{\rm core}^3, & r \le R_{\rm core}, \\ -GM_{\rm core}/r^2, & r > R_{\rm core}, \end{cases} \tag{3}$$

with the core radius $R_{\rm core}$, we determine the density distribution of the red giant envelope; see Appendix A for details. For the equation of state, we assume the polytrope of $P = K\rho^{(1+1/N)}$ with the polytropic index $N = 1.5$, which corresponds to the adiabatic equation of state with the adiabatic exponent $\Gamma = 5/3$; the polytropic constant K stands for the specific entropy of the monatomic ideal gas.

Figure 1 shows the density distributions in the envelope of red giants, thus obtained, for the models with different surface radii of $R_{\rm rg} = 20$ and $85\ R_\odot$. When the radius and the density are normalized with the surface radii $R_{\rm rg}$ and the envelope density $\rho_{\rm env} = M_{\rm env}/R_{\rm rg}^3$, two density distributions become nearly identical except inside of the core, which is a feature of red giant structure unless the mass in the envelope is much smaller than the core mass (Fujimoto & Tomisaka 1992). In this figure we also plot the density distribution in the red giant by taking the model from the evolutionary calculation (Suda & Fujimoto 2006) for comparison, which exemplifies that the analytic models can reproduce the envelope structure of red giants very well. Moreover, we compare the models with different core radii of $R_{\rm core} = 0.026$ and $2\ R_\odot$ to demonstrate that the assumed core radii hardly affect the structure outside the core of $r > 2\ R_\odot$ and, in particular, in the outer envelope that may take a main part in tidal deformations, while the central density differs greatly by a factor of 4.6×10^5. In our simulations, we therefore set $R_{\rm core} = 2\ R_\odot$ to reduce the number of particles injected into the innermost region. The initial models of red giants for the SPH simulation are constructed by distributing particles according to these envelope solutions and

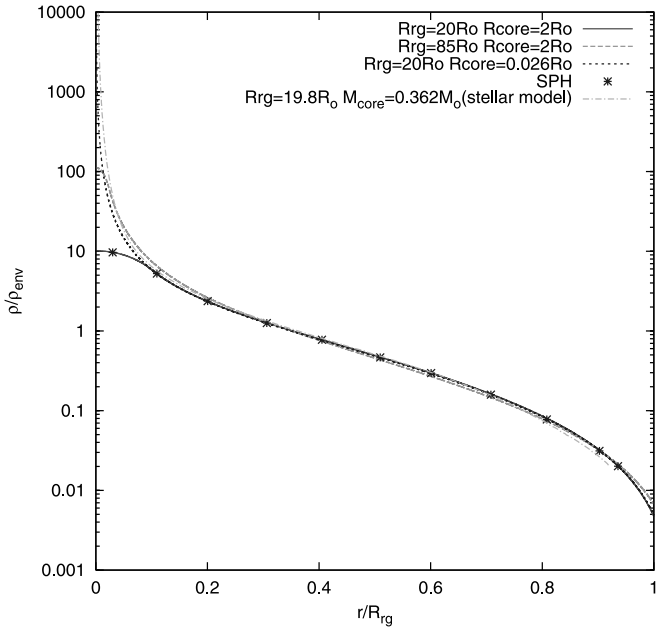

FIG. 1.—Distribution of density in the envelope of red giants, normalized with respect to the envelope mass and radius ($M_{\rm env} = R_{\rm rg} = 1$) as a function of normalized radius. Solid and long-dashed curves denote the models of the same core radius of $R_{\rm core} = 2\ R_\odot$ with the same total mass 0.8 $M_\odot$, different surface radii $R_{\rm rg} = 20$ and 85 $R_\odot$, and different core masses $M_{\rm core} = 0.32$ and 0.48 $M_\odot$, respectively, while dashed curve denotes the model with the same surface radius $R_{\rm rg} = 20\ R_\odot$ and the same core mass $M_{\rm core} = 0.32\ M_\odot$ with the same total mass 0.8 $M_\odot$ and a different core radius $R_{\rm core} = 0.026\ R_\odot$, for comparison. Dash-dotted curve denotes a stellar model of $R_{\rm rg} = 19.8\ R_\odot$ and $M_{\rm core} = 0.362\ M_\odot$, taken from the evolutionary calculation of a star with mass 0.8 $M_\odot$ and the metallicity [Fe/H] = −1.5 by Suda & Fujimoto (2006). Asterisks represent the density distribution of the SPH model with $R_{\rm rg} = 20\ R_\odot$ for the radii at intervals of 2 $R_\odot$ with two additional ones near the center and surface. [*See the electronic edition of the Journal for a color version of this figure.*]

then by relaxing them into hydrostatic equilibrium with an artificial damping force on the particles. The relaxed distribution of SPH particles is also shown in the figure; it reproduces the structure of the red giant envelope very well except for the very surface layer of mass less than ∼0.0001 $M_\odot$ because of mass resolutions, where the variable smoothing length, h, $\sim 0.1 R_{\rm rg}$.

2.3. *Accretion onto the Main-Sequence Star*

We assume that the main-sequence star, treated as a point mass perturber, accretes any SPH gas particles that enter within the accretion radius, $r_{\rm acc}$, which is defined as half the Roche lobe radius, R_L, calculated under the assumption of a circular orbit at an instantaneous separation, D, between the main-sequence star and the red giant, and is given by

$$r_{\rm acc} = 0.5 R_L = 0.5 D(0.38 + 0.2 \log q), \tag{4}$$

in which the expression for R_L is valid for the mass ratio $0.3 < q = M_{\rm ms}/M_{\rm rg} < 20$ (Paczynski 1971). A factor of 0.5 is adopted in order for the main-sequence star not to artificially accrete unbound particles that happen to enter its Roche lobe. We have confirmed that the number of accreted particles is nearly the same with a smaller accretion radius $r_{\rm acc} = 0.1 R_L$. As for the accreted SPH particles, the mass, momentum, and angular momentum that they carry are added to the point mass of the main-sequence stars.

3. RESULTS OF SIMULATIONS

We have carried out 25 simulations of a tidal encounter with a red giant of mass 0.8 $M_\odot$ and a main-sequence star by varying the impact parameter, b, for eight sets of parameter combinations with the two different red giant models, the two different main-sequence stars, and the two choices of artificial viscosity parameters. The model parameters are summarized with model identifiers in Table 1. We adopt relatively heavy main-sequence stars of mass 0.8 and 0.6 $M_\odot$, based on the fact that the mass segregation may proceed to enhance the abundance of relatively massive stars in the cluster cores where the close encounters are expected to occur more frequently because of larger stellar density. In this table we give the periastron distance, r_p, instead of the impact parameter b, which is given for a hyperbolic orbit as

$$b^2 = r_p^2 \left[1 + 2G(M_{\rm rg} + M_{\rm ms})/r_p v_\infty^2\right], \tag{5}$$

where v_∞ is the relative velocity before the encounter and is set to be $v_\infty = 10$ km s^{-1} in the present work. We also define the ratio, η, between the critical angular velocity, $\Omega_{\rm rg}$, of rotation at the initial surface of the red giant and the angular velocity, $\Omega_{\rm pass}$, for the circular orbit at the periastron distance, r_p, as a measure of the closeness of encounter,

$$\eta = \frac{\Omega_{\rm rg}}{\Omega_{\rm pass}} = \left(\frac{M_{\rm rg}}{M_{\rm rg} + M_{\rm ms}}\right)^{1/2} \left(\frac{r_p}{R_{\rm rg}}\right)^{3/2}, \tag{6}$$

following Press & Teukolsky (1977). In addition, we give the characteristic results of simulations, the energy and angular momentum transferred into the red giants from the orbital motions and the masses accreted onto the main-sequence stars and lost from the systems; also listed are the periods, semimajor axes, and eccentricities of orbital motions for the models that yield bound systems, and the models that end up with positive orbital energy are denoted as flyby.

Figure 2 gives the snapshots showing the variations of surface density, Σ, projected on the orbital plane for model a8rg1 ($R_{\rm rg} = 20\ R_\odot$, $M_{\rm ms} = 0.8\ M_\odot$, $\alpha_{\rm SPH} = 1.0$, $r_p/R_{\rm rg} = 1.75$ or $\eta = 1.64$); the contours, separated by 0.2 dex, are plotted in the range of 10–0.001 times the average surface density, $\Sigma_{\rm env} = M_{\rm env}/\pi R_{\rm rg}^2$, and open circles denote the accretion radius of the main-sequence star. Numerals in the right bottom corner give the elapsed time from the onset of the simulation in units of the dynamical timescale, $\tau_{\rm rg} = (R_{\rm rg}^3/GM_{\rm env})^{1/2}$, defined with the envelope mass of the red giant as in Davies et al. (1991). On each panel, open and filled squares mark the gas particles, initially situated on two separate shells on the orbital plane, as indicators of stellar rotation.

As the main-sequence star approaches, the tidal bulge is raised on the surface layer of the red giant and grows toward the main-sequence star. The oscillations of $l = 2$ f-modes are predominantly excited as predicted from the linear perturbation theory. In the outer shells of a few 10% in mass fraction, the deformations greatly elongated toward the perturber develop into the nonlinear regime, as seen from the filled squares; in the interior, on the other hand, the perturbations remain small in the linear regime, as observed from the location of the open squares, and the gas almost stays at rest in the still, deep interior. The outer deformations cannot keep pace with the motion of the perturber, as it is accelerated because the timescale of passage of the perturber is comparable to that of oscillatory motions and the rotation rate of the red giant is initially small. The lag of tide develops as

TABLE 1

PARAMETERS AND CHARACTERISTIC RESULTS OF ENCOUNTER SIMULATIONS

Model	α_{SPH}	M_{ms} ($M_\odot$)	r_p (R_{rg})	η	$\Delta E(t_E)$ (GM_{rg}^2/R_{rg})	$\Delta L_{rg}(t_E)$ ($M_{rg}R_{rg}^2\Omega_K$)	$M_{acc}(t_E)$ ($M_\odot$)	$M_{loss}(t_E)$ ($M_\odot$)	T_{orb} (yr)	e	a (AU)
Red Giant Model of $R_{rg} = 20\ R_\odot$											
a8rg1	1.0	0.8	1.75	1.64	1.86E−2	2.6E−2	6.70E−3	5.09E−4	4.19	0.95	3.04
b8rg1	1.0	0.8	2.00	2.00	8.19E−3	9.2E−3	2.91E−3	1.92E−5	22.99	0.98	9.4
c8rg1	1.0	0.8	2.25	2.40	3.09E−3	3.8E−3	5.47E−4	0.0	Flyby	...	...
d8rg1	1.0	0.8	2.50	2.80	9.48E−4	1.4E−3	0.0	0.0	Flyby	...	...
e8rg1	0.1	0.8	1.75	1.64	1.88E−2	2.6E−2	6.93E−3	5.47E−4	4.09	0.95	2.99
f8rg1	0.1	0.8	2.00	2.00	8.32E−3	9.2E−3	2.97E−3	4.80E−5	22.01	0.98	9.17
g8rg1	0.1	0.8	2.25	2.40	3.19E−3	3.9E−3	5.37E−4	9.60E−6	Flyby	...	...
h8rg1	0.1	0.8	2.50	2.80	1.00E−3	1.4E−3	0.0	0.0	Flyby	...	...
a6rg1	1.0	0.6	1.50	1.40	2.35E−2	3.3E−2	5.81E−3	1.14E−3	1.86	0.92	1.69
b6rg1	1.0	0.6	1.75	1.75	1.12E−2	1.4E−2	2.95E−3	1.44E−4	7.25	0.96	4.18
c6rg1	1.0	0.6	2.00	2.14	4.33E−3	5.0E−3	8.06E−4	9.60E−6	91.9	0.99	22.8
d6rg1	1.0	0.6	2.25	2.55	1.41E−3	1.9E−3	9.60E−6	0.0	Flyby	...	...
e6rg1	0.1	0.6	1.50	1.40	2.37E−2	3.3E−2	5.97E−3	0.0	Flyby	...	...
Red Giant Model of $R_{rg} = 85\ R_\odot$											
a8rg2	1.0	0.8	1.41	1.18	2.49E−2	3.3E−2	6.66E−3	2.22E−3	60.3	0.97	18.0
b8rg2	1.0	0.8	1.80	1.70	9.29E−3	1.1E−2	3.20E−3	2.50E−4	Flyby	...	...
c8rg2	1.0	0.8	1.88	1.82	7.18E−3	9.3E−3	2.51E−3	1.82E−4	Flyby	...	...
d8rg2	1.0	0.8	2.00	2.00	4.71E−3	5.2E−3	1.57E−3	5.02E−6	Flyby	...	...
e8rg2	1.0	0.8	2.12	2.18	3.25E−3	3.5E−3	8.83E−4	1.28E−5	Flyby	...	...
f8rg2	1.0	0.8	2.45	2.71	8.79E−4	1.1E−3	1.92E−5	0.0	Flyby	...	...
g8rg2	0.1	0.8	1.41	1.18	2.49E−2	3.3E−2	6.66E−3	2.22E−3	60.3	0.97	1.80
h8rg2	0.1	0.8	1.80	1.70	9.18E−3	1.1E−2	3.52E−3	2.24E−4	Flyby	...	...
i8rg2	0.1	0.8	2.00	2.00	4.71E−3	5.5E−3	1.56E−3	6.4E−6	Flyby	...	...
a6rg2	1.0	0.6	1.41	1.27	1.68E−2	2.3E−2	3.56E−3	1.13E−3	142.2	0.98	3.04
b6rg2	1.0	0.6	1.65	1.60	8.84E−3	1.2E−2	2.20E−3	3.26E−4	Flyby	...	...
c6rg2	1.0	0.6	1.88	1.95	4.11E−3	4.8E−3	4.80E−4	2.56E−4	Flyby	...	...

the perturber approaches the periastron. Later around a time of 6.5 τ_{rg} after the periastron passage, the gas streaming out of the red giant starts to accrete onto the main-sequence star, now separated by $D \simeq 4R_{rg}$.

At the same time, there appears an interesting nonlinear feature in the vicinity of the surface of the red giant star. As a result of the $l = 2$, f-mode oscillations, a density ditch is formed near the interface of upward and downward motions, as seen from the panels in the middle row of Figure 2. Figure 3 shows an enlarged picture of the velocity structure when the ditch is formed. Since the expanded mass elements gain larger tidal torque than the compressed mass elements, the former overtakes the latter while contracting to form an eddylike velocity structure of counterclockwise rotation. The rotation of Lagrangian shells and the resultant deposition of angular momentum into the red giant star due to the tidal torque proceed spectacularly in the surface region, dominated by the nonlinear effects. Such features can no longer be the case in the linear theory, although the mass involved in the nonlinear deformations is small, as seen from the movement of the open squares. Similar nonlinear effects are reported by Khokhlov et al. (1993a) who study tidal encounters between a polytropic star and a black hole, although they assume large periastron distances, and hence, the deformations remain nearly axial symmetric without mass transfer, which is different from our case.

This model illustrates an example that ends with the formation of a bound system after the encounter, as seen from Table 1. In model e8rg1 with the same parameters but for the smaller shear viscosity of $\alpha_{SPH} = 0.1$, the deformations are identical during the earlier phase of time 0–5τ_{rg} to those in Figure 2, and the effect of smaller viscosity is plainly discernible only in the deeper ditch that develops after six time units. Accordingly, there are only small differences in the results in Table 1. This suggests that the transfer of energy and angular momentum is attributed solely to the phase lag of the deformations, dynamically generated in the red giant envelope behind the perturber passage. The interactions to exchange these quantities predominantly occur near the periastron passage of the smallest separation while the deformations are still growing. On the other hand, the effects of viscosity become important only after the deformations contract to generate a strong shear near the stellar surface, and hence, the value of viscosity hardly affects the transfer characteristics.

The models of larger impact parameters such as model c8rg1 of $\eta = 2.4$ result in a flyby encounter. The nonlinear deformations in the outer shells of the red giant are weaker than those of the model of the closer encounter $\eta = 1.64$ in Figure 2. Because of the slower angular velocity of the perturber, the tidal bulge stretched out toward the perturber is relatively slimmer to form a chimneylike structure. The ditch and the eddylike structure, generated on the surface, are also in smaller scales.

The encounter with a less massive perturber results in smaller transfer characteristics, a part of which is due to a larger periastron passing time, η, when compared at the same periastron distance. Model c6rg1 of $M_{ms} = 0.6\ M_\odot$ and $r_p = 2.00R_{rg}$ ($\eta = 2.14$) exhibits a similar chimneylike structure as model b8rg1 of the massive perturber with the same periastron distance, but the surface deformations are slightly smaller because of larger η. The overall transfer characteristics lie between those of two massive

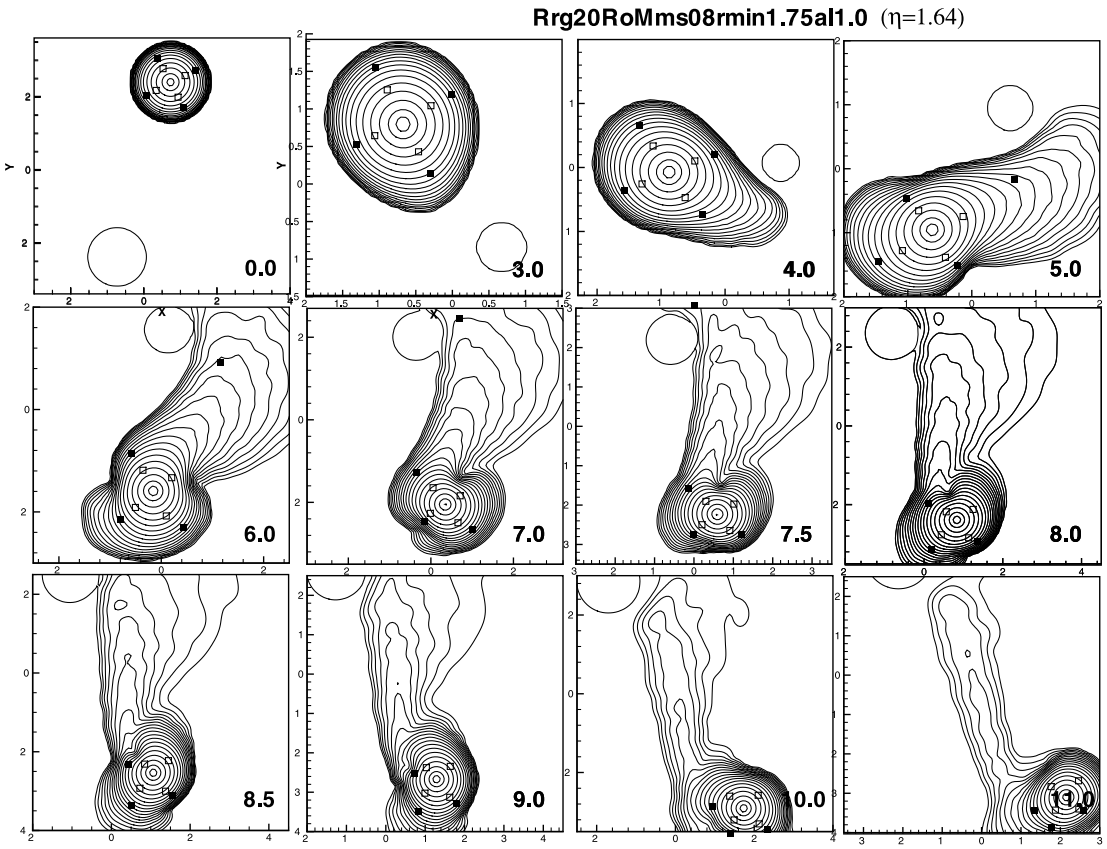

FIG. 2.—Variations in the surface density, projected on the orbital plane, during the encounter for case a8rg1 ($R_{rg} = 20\ R_\odot$, $\eta = 1.64$, $M_{ms} = 0.8\ M_\odot$, and $\alpha = 1.0$). Each panel shows a snapshot of contour lines at intervals of 0.2 dex in the logarithmic scale over the range of 10–0.001 times the average surface density, $\Sigma_{env} = M_{env}/\pi R_{rg}^2$. The origin is set at the center of mass, and numerals in the right bottom corner indicate the time in units of dynamical timescale, $\tau_{rg} = (R_{rg}^3/GM_{env})^{1/2}$. Filled and open squares indicate representative SPH particles initially located on the shells that contain 95% and 70% of total mass including the core mass in the interior, respectively.

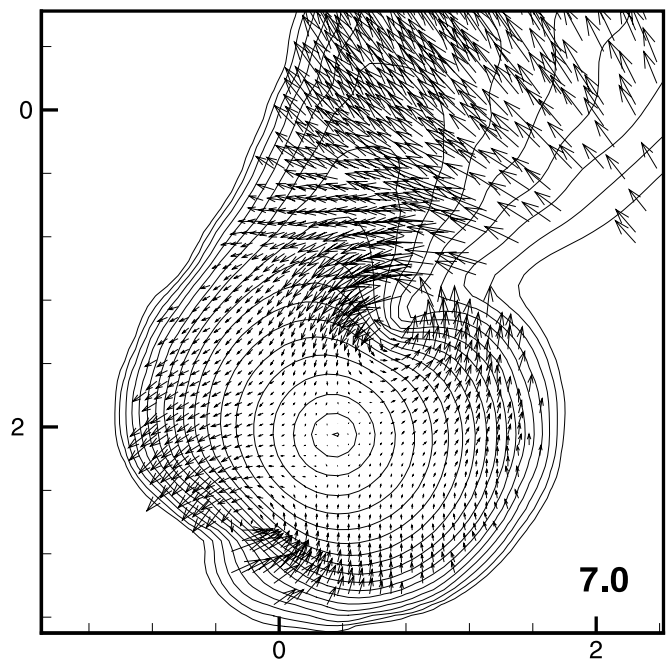

FIG. 3.—Velocity vectors, plotted on the density contour map of the panel at time $7.0\tau_{rg}$ from Fig. 2.

perturber models, model b8rg1 with $\eta = 2.00$ and model c8rg1 with $\eta = 2.40$.

The encounters with red giants at later evolutionary stages are exemplified by the models of the larger radius, $R_{rg} = 85\ R_\odot$. When models with the same encounter closeness parameter η are compared, the overall characteristics of interaction, i.e., the structure of mode oscillations, the development of deformations, and the accretion process, are very similar in all models, despite the large difference in the physical distance scales. This is attributable to the nature of the envelope structure of red giants, i.e., to the self-similar density structure, as shown in Figure 1. The resultant transfer characteristics also turn out to be very similar when we subtract the effects of the smaller envelope mass.

The overall features of gas streaming are as follows. For small periastron distances as in these encounters, the nonlinear effects in the tidal interactions are important and the surface density profile becomes highly asymmetric in the outer shells of red giants. As the perturber approaches the periastron, the tidal bulge is excited in the red giant and elongated, first directed to the perturber. Since it cannot catch up with the motion of the perturber because of initially slow rotation, gas particles from the surface of the red giant chase after the perturber to gain the energy and angular momentum. Some of them eventually get captured by the gravitational potential of the perturber after the periastron passage. On the other hand, most of gas involved in the tidal bulge falls back onto the red giant with gained angular momentum, which produces a nonlinear feature of eddylike structure in the surface region. Even in the case of binary formations, the orbit is highly

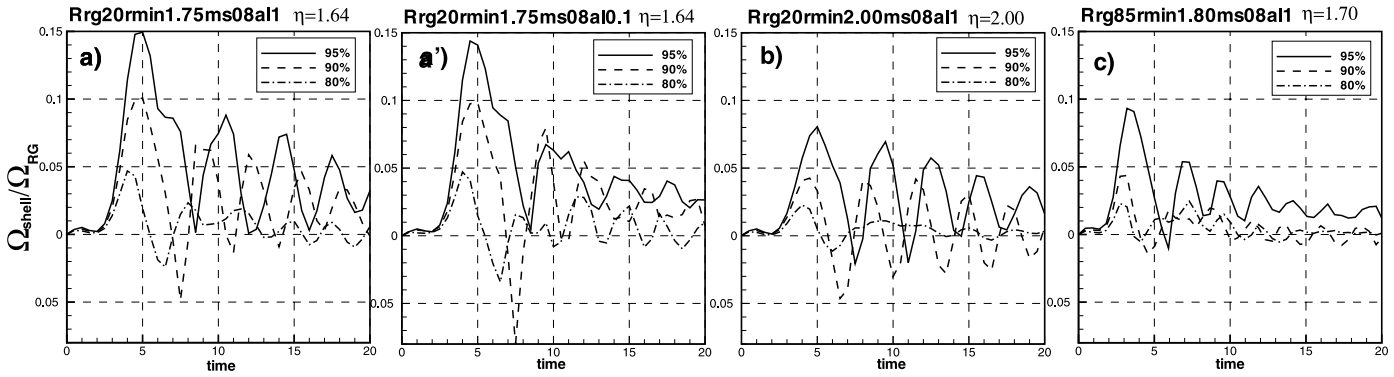

FIG. 4.—Time variations of angular velocity, $\Omega_{\rm shell}$, averaged over particles in Lagrangian rings on the $z = 0$ orbital plane, initially located at the shells, the interior of which contains 95%, 90%, and 80% of the mass of the red giant (including the core mass); the vertical axis is the angular velocity normalized with respect to the Keplerian value at the initial surface [$\Omega_{\rm rg} = (GM_{\rm rg}/R_{\rm rg}^3)^{1/2}$], and the horizontal axis is time in units of $\tau_{\rm rg} = 1/\Omega_{\rm rg}$. (*a*) Model a8rg1; (*a′*, *b*) Models e8rg1 and b8rg1, which differ from (*a*) in the viscous parameter and in the encounter closeness parameter, respectively; (*c*) Model b8rg2 with the red giant model of larger surface radius.

eccentric, and hence, as two stars go away from each other the tidal bulge becomes slender.

3.1. *Nonlinear Deformations and the Evolution of Differential Rotation*

The transfer of orbital energy and angular momentum to the red giant is characterized by the following three timescales: (1) the periastron passing timescale of the main-sequence star, $\tau_{\rm pass}$ ($=1/\Omega_{\rm pass}$), which is related to the variation of the external perturbing force; (2) the dynamical timescale of the envelope of the red giant, $\tau_{\rm dyn}$ ($=1/\Omega_{\rm rg}$), which is related to the stellar oscillations in response to the external force; and (3) the viscous timescale in the envelope of the red giant, $\tau_{\rm vis}$ ($=R_{\rm rg}^2/\nu_{\rm eddy}$), which is caused by the convective eddy in the red giant envelope. In our case, $\tau_{\rm dyn} \lesssim \tau_{\rm pass} \ll \tau_{\rm vis}$. For a slowly rotating red giant, the tidal bulge tends to fall behind the accelerated motion of the perturber, and hence, a tidal lag is formed dynamically to carry the energy and angular momentum from the orbital motion into the oscillatory motions and rotation of the red giant envelope. The viscosity plays secondary roles in the transfer of energy and angular momentum, as seen in Table 1. The accreted mass also depends little on the assumption of viscosity. Furthermore, we see that the accreted mass takes nearly the same values regardless of the difference in the red giant models when compared among the models with similar values of $\Delta E/(GM_{\rm rg}^2/R_{\rm rg})$, instead of the encounter closeness parameter η. This is indicative that the mass accretion is determined by the same process of energy deposition.

Figure 4 shows the time variations of angular velocity, $\Omega_{\rm shell}$, relative to its Keplerian angular velocity, $\Omega_{\rm rg} = (GM_{\rm rg}/R_{\rm rg}^3)^{1/2}$, averaged over the gas particles in the three Lagrangian rings on the orbital plane, initially located at the shells which contain 95%, 90%, and 80% of the mass of the red giant (including the core mass). The tidal torque excites the oscillations of $\Omega_{\rm shell}$ of periods $\sim 2\tau_{\rm rg}$, corresponding to the $l = 2, m = \pm 2$ *f*-mode. As the perturber approaches, the oscillations develop precipitously to reach the maximum strength near the periastron passage (at $t \simeq 4.5\tau_{\rm rg}$ and $3.0\tau_{\rm rg}$ for the models with $R_{\rm rg} = 20$ and 85 $R_\odot$, respectively) with greater amplitudes and longer durations in the outer shells. Accordingly, the turnover of rotation velocity is delayed in the outer shell, and at the same time, the mean rotation velocity of oscillation increases in the prograde direction, reflecting the injection of angular momentum due to the tidal torque, which is stronger in outer shells. The amplitudes and mean values of oscillations are greater for closer encounters. Between the different red giant models with the same closeness parameter η, the model with the larger radius entails smaller variations in the rotation rate, normalized with respect to the characteristic rotation rate, $\Omega_{\rm shell}/\Omega_{\rm rg}$; this is true even if we take into account the fact that the shell of the same mass fraction is 50% deeper in the envelope because of the smaller envelope mass. It should be noted however that the net amount of angular momentum transferred is larger, although only slightly, for the red giant model of larger radius because of the larger critical angular momentum ($R_{\rm rg}^2\Omega_{\rm rg}$).

As for the effects of viscosity on the time variations of $\Omega_{\rm shell}$, the largest one appears in the difference in the minimum value after the periastron passage; for the smaller viscous parameter, it decreases to be smaller, and along with the phase delay of outer shells, the eddylike structure of counterclockwise flow becomes stronger, as stated above. The time of minimum $\Omega_{\rm shell}$ coincides nearly with the time of the strongest eddy in Figure 2. Stronger shear produced by the eddylike structure in turn enhances the dissipation and inward transport of angular momentum; in Figures 2*a* and 2*a′* we see the amplitudes of oscillations in the outer two shells get smaller in the second and later cycles for the models of smaller viscosity, although the overall similarity holds, in particular, in the shifts of mean values of oscillations.

Figure 5 illustrates the evolution of the radial distribution of angular velocity, averaged over the gas particles between cylinders, perpendicular to the orbital plane, with the outer and inner radii separated by $0.1R_{\rm rg}$. The outermost layer is first accelerated and pulled the most outward to run after the perturber of angular velocity $\Omega_{\rm pass}$ at the periastron passage ($\simeq 0.61\Omega_{\rm rg}$ around the time $\sim 6\tau_{\rm rg}$). Then the deposited angular momentum is redistributed gradually into the interior. By $\sim 40\tau_{\rm rg}$, most of the interior up to the radius $R \simeq 1.1R_{\rm rg}$ tends to rotate uniformly while there remains differential rotation in the outer expanded layer of lower density. For the smaller viscosity parameter of $\alpha = 0.1$, the viscous process works slightly more slowly, and a uniform rotation is reached only in the interior of $R \lesssim 0.8R_{\rm rg}$ by $\sim 40\tau_{\rm rg}$ with stronger differential rotation in the outer shells. The timescale for the transfer of angular momentum inside the red giants is shorter than that estimated from the eddy viscosity, the latter of which is ~ 1 yr and 10 yr for the case of $\alpha_{\rm SPH} = 1.0$ and 0.1, respectively, while $\tau_{\rm rg} = 0.02$ yr. This also indicates that the nonlinear effects, seen from Figure 3, must mainly contribute to the redistribution of the angular momentum.

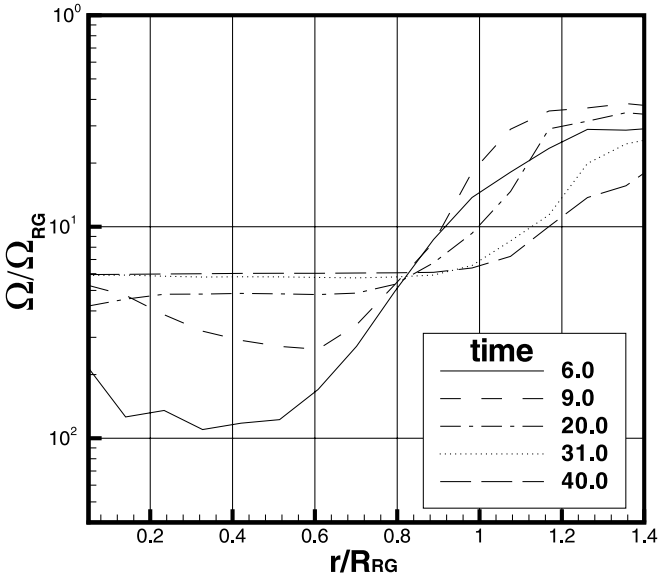

FIG. 5.—Evolution of radial distribution of angular velocity, averaged over the particles that reside temporally between the cylinders, separated by $0.1R_{\rm rg}$ on the orbital plane, for model b8rg1; $\Omega_{\rm rg}$ [$=(GM_{\rm rg}/R_{\rm rg}^3)^{1/2}$] is the critical rotation velocity at the initial surface of the red giant, and the time is designated in the box in units of dynamical time of $\tau_{\rm rg} = (R_{\rm rg}^3/GM_{\rm env})^{1/2}$.

3.2. *Transfer of Energy and Angular Momentum and Mass Accretion*

We evaluate the change in the orbital energy, ΔE, from the difference of the kinetic and potential energy as

$$\Delta E(t) = \frac{1}{2}\mu_0 v_\infty^2 - \left(\frac{1}{2}\mu v^2 - \frac{GM_{\rm rg}M_{\rm ms}}{r}\right), \qquad (7)$$

where μ is the reduced mass, r and v are the relative distance and velocity, respectively, and the subscript 0 denotes the quantities before the encounter. We may well assume that the change in the orbital energy is equal to the energy transferred to the red giant, since the energy carried away by the particles that escape from the system is much smaller and escaped mass is smaller than accreted mass by nearly an order of magnitude as seen from Table 1.

The total angular momentum, ΔL, transferred into the red giant is estimated by summing up the specific angular momentum for all the particles constituting the red giant envelope around the core,

$$\Delta L(t) = \sum_i m_i(\boldsymbol{r}_i - \boldsymbol{r}_{\rm rg})(\boldsymbol{v}_i - \boldsymbol{v}_{\rm rg}), \qquad (8)$$

where m_i, $\boldsymbol{r}_i$, and $\boldsymbol{v}_i$ are respectively the mass of the ith gas particle and its position and velocity vectors, and $\boldsymbol{r}_{\rm rg}$ and $\boldsymbol{v}_{\rm rg}$ are the position and velocity vectors of the core of the red giant, respectively. We exclude from the summation the gas particles which have accreted onto the main-sequence star and those which have escaped from the system; the latter particles are defined as satisfying the following two conditions: (1) the total energy, i.e., the sum of the thermal, kinetic, and potential energy, of a gas particle is positive; and (2) the radial velocity is positive when measured from the center of mass.

Figures 6 and 7 show the time variations of orbital energy and angular momentum ($E_{\rm orb} = \mu_0 v_\infty^2 - \Delta E$ and $L_{\rm orb} = \mu_0 b v_\infty - \Delta L$), respectively, for the 20 $R_\odot$ models. As the periastron is approached, both decrease rapidly and reach the minimum after the periastron passage. Then, they turn to increase gradually to resume the loss of up to $\sim$28% in the largest case and approach

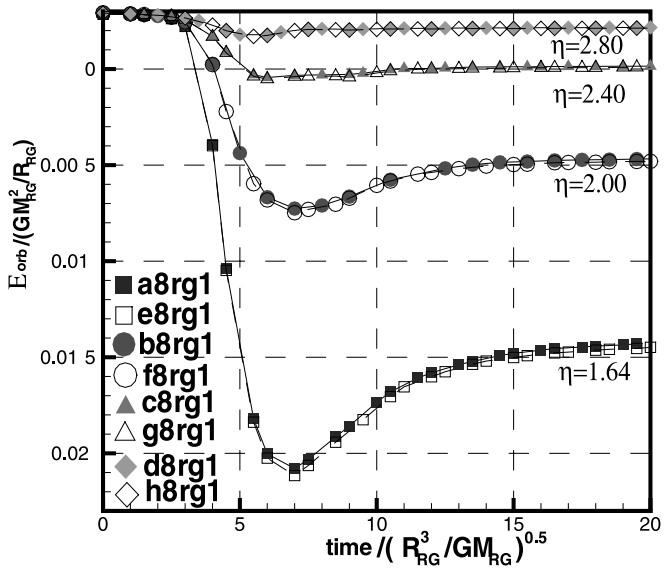

FIG. 6.—Time variations in the orbital energy, $E_{\rm orb} = (1/2)\mu_0 v_\infty^2 - \Delta E$. Filled and open symbols denote the models of $\alpha_{\rm SPH} = 1.0$ and 0.1, respectively. A legend for the symbols is provided in the figure.

asymptotic constant values. Figure 8 shows the time variation of mass, $M_{\rm acc}$, trapped by the perturber; the beginning of mass accretion coincides with when the orbital energy and angular momentum hit the minimum, and the increase in the accreted mass follows the curves of the latter's recovery. This indicates that the orbital energy and angular momentum once received by the surface matter are slowly returned back to the orbital motion by the accretion process.

At the end of our simulations, the motions of the two stars tend to settle in asymptotic orbits, and the characteristics no longer change. We present the values of $\Delta E(t_E)$, $\Delta L(t_E)$, and $M_{\rm acc}(t_E)$ at the end of our simulation at $t = t_E = 20\tau_{\rm rg}$ or $40\tau_{\rm rg}$ in Table 1. The deposited energy and angular momentum into the red giant envelope increase precipitously with decreasing periastron distance, and for $r_p \lesssim 2R_{\rm rg}$, both of them become appreciable in comparison with the gravitational binding energy and the angular

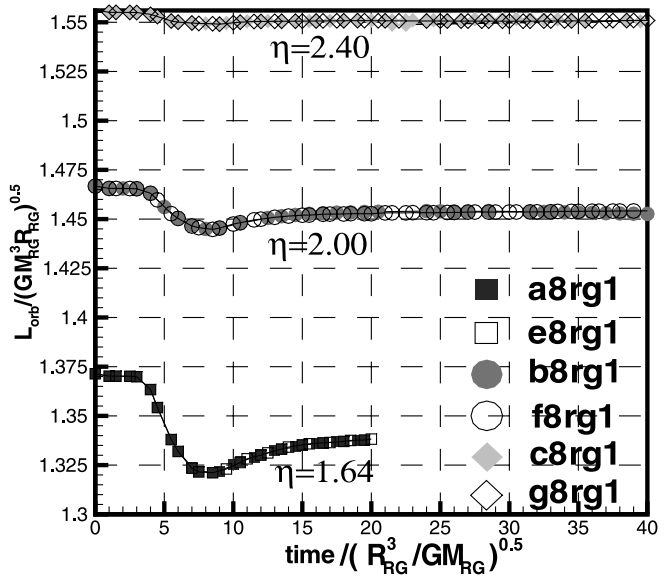

FIG. 7.—Time variations in the orbital angular momentum, $L_{\rm orb} = \mu_0 b v_\infty - \Delta L_{\rm rg}$. A legend for the symbols is provided in the figure.

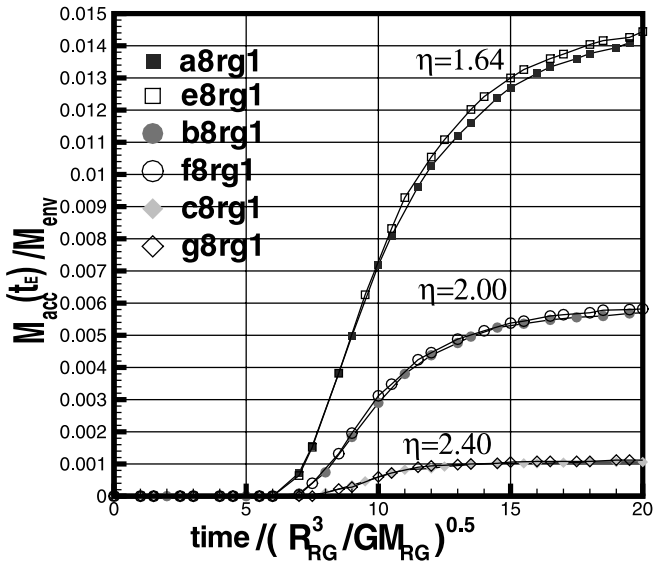

FIG. 8.—Time variations of the accreted mass, M_{acc}, onto the secondary point mass. Symbols have the same meanings as in Fig. 7.

momentum corresponding to the critical rotation of red giants, respectively. The angular momentum of $\Delta L(t_E) \gtrsim 0.01 I_{rg}\Omega_{rg}$ (where I_{rg} is the moment of inertia of the red giant) can be deposited, which is necessary to explain such fast rotators as observed for the HB stars in the globular clusters. The accreted mass onto the main-sequence stars also shows a similar tendency, amounting to be comparable with the mass in the surface convective zone of main-sequence stars near the turnoff stars in the globular clusters ($\sim$0.003 $M_\odot$; see, e.g., Suda & Fujimoto 2006). As the perturber mass decreases by 25% from $M_{ms} = 0.8$ to 0.6 $M_\odot$, the deposited energy and angular momentum decrease by a factor of 1.6–2.2, and the accreted mass decreases by a slightly larger factor of 2.3–2.5. When the two red giant models are compared at the same encounter closeness parameter η, the interactions tend to be weaker for red giant models of larger radius, when normalized with respect to their radii, giving smaller $\Delta E(t_E)/(GM_{rg}^2/R_{rg})$ and $\Delta L(t_E)/(GM_{rg}^3 R_{rg})^{1/2}$, although the differences remain less than a factor of 2. This is attributable mainly to the smaller envelope mass involved in the tidal deformations (decreasing by 50%) for the model of the larger radius.

In our simulations the border between the tidal capture and the flyby, i.e., whether two stars form a bound system or fly apart after the encounter, lies in the range of $2.14 < r_p/R_{rg} < 2.25$ for 20 $R_\odot$ and $1.41 < r_p/R_{rg} < 1.65$ for 85 $R_\odot$, respectively. Our tidal capture limit is somewhat larger than that obtained from the linear analysis by McMillan et al. (1990) who give the range $r_p/R_{rg} = 1.5$–1.7 for the capture of a 0.5 $M_\odot$ dwarf (see Table 2) and Bailyn (1988) who give the range $r_p/R_{rg} = 1.0$–2.0 for the capture of a 1.4 $M_\odot$ neutron star. As for the dependence on the red giant models, the case of 85 $R_\odot$ results in the flyby for closer encounters than the case of 20 $R_\odot$ when compared between the models of the same periastron distance normalized by the stellar radius. This is due to the smaller binding energy of the envelope, which directly affects the capture condition $\Delta E(t_E) > (1/2)\mu_0 v_\infty^2$, as already discernible in the linear analysis by McMillan et al. (1990). On the other hand, a larger radius causes relatively greater effects on the angular momentum deposition and mass accretion; for the red giants of late evolutionary stages, even the flyby encounters can give sufficient amounts of angular momentum and accreted mass to explain the fast rotators of HB stars and to disguise the surface of the main-sequence star with accreted matter.

TABLE 2
TIDAL CAPTURE LIMITS

M_{ms} ($M_\odot$)	R_{rg} ($R_\odot$)	η_{cap}	$r_{p_{cap}}$ (R_{rg})	η_{cap}^{linear}	$r_{p_{cap}}^{linear}$ (R_{rg})
0.6.....	20	2.3	2.1	1.78	1.77
0.8.....	20	2.38	2.25	1.82	1.88
1.4.....	20	2.47	2.56	1.91	2.16
0.6.....	85	1.5	1.58	1.14	1.31
0.8.....	85	1.58	1.71	1.20	1.42
1.4.....	85	1.70	2.00	1.31	1.68

NOTES.—First and second columns are main-sequence mass and red giant radius. Third and forth ones are η and r_p at tidal capture limit for parameters of first and second columns estimated from our simulations. Last two columns are same as that of third and forth ones but are estimated from linear theory.

4. PARAMETER DEPENDENCES OF TRANSFER CHARACTERISTICS AND FITTING FORMULAE

4.1. *Tidal Energy Deposition and Angular Momentum Transfer*

The linear perturbation theory has been developed by Press & Teukolsky (1977) and Lai (1997) to evaluate the transfer of energy and angular momentum through the dynamical tides; according to their results, the parameter dependences of these quantities are given explicitly in equations (B7) and (B13) for the $l = 2$ f-modes (see Appendix B). In order to separate the effects of the secondary mass, we may define $\Delta\tilde{E}$ and $\Delta\tilde{L}$ as

$$\Delta\tilde{E} \equiv \Delta E(t_E)/\left\{\left(GM_{rg}^2/R_{rg}\right)\left[M_{ms}/(M_{rg}+M_{ms})\right]^2\right\}, \quad (9)$$

$$\Delta\tilde{L} \equiv \Delta L(t_E)/\left\{\left(M_{rg}R_{rg}^2\Omega_{rg}\right)/\left[M_{ms}/(M_{rg}+M_{ms})\right]^2\right\}. \quad (10)$$

In the linear theory, $\Delta\tilde{E}$ and $\Delta\tilde{L}$ are expressed in terms of the transfer functions, $T_2(\eta; Q_{02}, \omega_{02})$ and $S_2(\eta; Q_{02}, \omega_{02})$, given in equations (B8) and (B14) in Appendix B, respectively; here ω_{02} and Q_{02} are the frequency and overlap integral of $l = 2$, f-mode oscillations and, for the red giants, are given by interpolation formulae of equations (B10) and (B9) in Appendix B as a function of radius. Since the $l = 2$ modes dominate over the oscillatory motions even in the nonlinear regime, we may utilize these transfer functions and seek the fitting formulae of $\Delta\tilde{E}$ and $\Delta\tilde{L}$ as a function of η for the given models of red giants.

Further, the transfer characteristics obtained by the numerical simulations differ also with the internal structure of red giant models, as seen above. In the linear theory, the dependences of the internal structure are included in the transfer functions, in particular, through the overlap integral Q_{02}. In the tidal interactions via the torque, the coupling is given by the moment of inertia of the envelope, since the core acts as an inert source of gravity. As a corollary, the transfer functions can be scaled with the inertia of the envelope. We define the nondimensional moment of inertia, $\tilde{I}$, as

$$\tilde{I} \equiv \int 4\pi r^4 \rho\, dr/M_{rg}R_{rg}^2 \simeq 0.15(M_{env}/M_{rg}), \quad (11)$$

for the red giant models. The approximation in the rightmost member in equation (11) follows from the similarity of the envelope structure in the red giants when normalized with respect to the surface radius and the envelope mass, as shown in Figure 1. For a main-sequence model of polytrope $N = 1.5$, we have $\tilde{I} \equiv \int 4\pi r^4 \rho\, dr/M_{ms}R_{ms}^2 \simeq 0.2$.

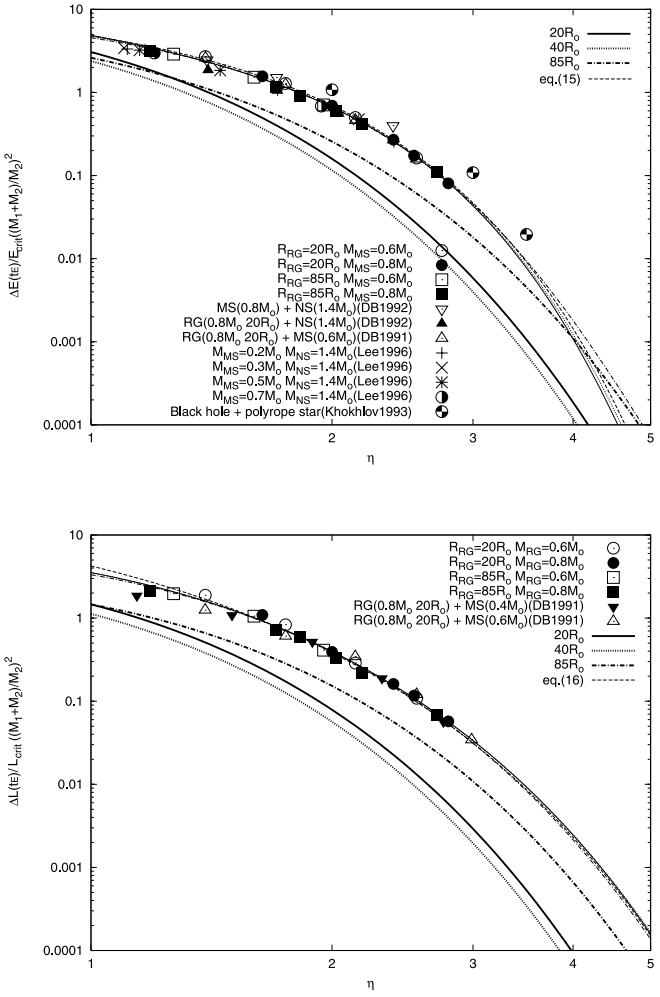

FIG. 9.—Deposited energy and angular momentum, normalized by the inertia, $\Delta\tilde{E}/0.5\tilde{I}$ (*top*) and $\Delta\tilde{L}/\tilde{I}$ (*bottom*) from the orbital to stellar internal motions are plotted as a function of the encounter closeness parameter η for the red giant models of radius 20 and 85 $R_\odot$ (*circles and squares*) with the main-sequence perturber of mass 0.6 and 0.8 $M_\odot$ (*open and filled symbols*). Also plotted are the results by other authors: a red giant of mass 0.8 $M_\odot$ and radius 20 $R_\odot$ with main-sequence stars of mass 0.4 and 0.6 $M_\odot$ and with a neutron star of mass 1.4 $M_\odot$ by Davies et al. (1991, 1992; *inverted filled, open, and filled triangles*); a 0.8 $M_\odot$ main-sequence star with a neutron star of mass 1.4 $M_\odot$ by Davies et al. (1992; *inverted open triangles*); 0.2, 0.3, 0.5, and 0.7 $M_\odot$ main-sequence stars with a 1.4 $M_\odot$ neutron star by Lee et al. (1996; *plus signs, crosses, asterisks, and waning moons*); a polytrope with a black hole by Khokhlov et al. (1993a, 1993b; *windmills*). Thin solid, dotted, and dash-dotted curves denote the fitting curves given in eqs. (12) and (13) for 20, 40, and 85 $R_\odot$, respectively, and the dashed curve denotes eqs. (15) and (16), while thick curves denote the corresponding results derived from the linear theory. See text for details.

Figure 9 shows $\Delta\tilde{E}/(\tilde{I}/2)$ and $\Delta\tilde{L}/\tilde{I}$ as a function of η for the models with the different red giant models of radii 20 and 85 $R_\odot$ (denoted by circles and squares, respectively) and with the different main-sequence stars of mass 0.6 and 0.8 $M_\odot$ (denoted by open and filled symbols, respectively). They form a single curve on each panel, independent not only of the perturber mass but also of the red giant models. The models computed by Davies et al. (1991, 1992) are also plotted in this figure; their models of a 0.8 $M_\odot$ red giant and 20 $R_\odot$ give very good agreement with ours for the encounter not only with a 0.6 $M_\odot$ main-sequence star (*open triangles*) but also with a 1.4 $M_\odot$ neutron star (*filled triangles*). The encounter with neutron stars results in slightly smaller energy deposition (about several tenths) for close encounters of $\eta \lesssim 2$, which is attributable to the larger accretion radius of the neutron star, since the accretion of larger mass onto the perturber returns a larger portion of energy from the outer elongated part of the red giant envelope to the orbital motion. As for the angular momentum, the deposition is slightly smaller in their red giant models at close encounters of $\eta < 2$ than in ours, which may stem from the difference in the criterion of mass-loss particles, giving a larger mass loss to their models, or from larger radii of red giant, used in the normalization, with taking into account the swell of the red giants during the encounter.

In the top panel of Figure 9 we also plot the results for the encounter simulations of main-sequence stars with a neutron star and with a black hole by Davies et al. (1992) and Lee et al. (1996) and for the encounter of a $N = 1.5$ main-sequence star with a black hole by Khokhlov et al. (1993a). We approximate the main-sequence star with a polytrope of index $N = 1.5$ and take $\tilde{I} = 0.2$. These models fall very closely along the same curve as our models and seemingly compose a single group despite the difference not only in the mass of the main-sequence stars but also in the mass ratio. The models by Lee et al. (1996) give slightly smaller values than those by Davies et al. (1992) which may stem from the different criteria and treatment of the particles that accrete onto the neutron star. The models by Khokhlov et al. (1993a) give slightly larger values than those by Davies et al. (1992) which may stem from the neglect of the accretion effect.

This convergence may be related to the fact that the ratio, $\eta\omega_{02}$, between the timescale of periastron passage and the timescale of envelope oscillations decreases to near unity in the nonlinear regime for small η. A similar tendency in which the dependence on the stellar models becomes weaker for smaller η is also discernible in equations (B7) and (B13) from the linear perturbation theory. These results for the linear regime are also plotted in this figure, and the comparison with the results of the nonlinear regime indicates that the latter effect enlarges the deposition of energy and angular momentum by a factor of several and up to 10, while it becomes saturated and slightly dwindles for smaller $\eta < 2$ because of the mass accretion onto the perturber.

We may take advantage of the convergence in the nonlinear regime to evaluate the transfer characteristics for other red giant models and to seek the fitting formulae that express $\Delta E(t_E)$ and $\Delta L(t_E)$ in terms of model parameters. We define the critical rotation energy and angular momentum of model stars as $E_{\rm crit} = (1/2)\tilde{I}(GM_{\rm rg}^2/R_{\rm rg})$ and $L_{\rm crit} = \tilde{I}M_{\rm rg}R_{\rm rg}^2\Omega_{\rm rg}^2$, respectively, with the dependence on the moment of inertia taken into account, and assume the following fitting formulae that converge to the results of linear theory for distant encounters,

$$\Delta E(t_E)\Big/\Big\{E_{\rm crit}\big[M_P/(M_{\rm rg}+M_P)\big]^2\Big\} = \big(2/\tilde{I}\big)\eta^{-4}T_2(\eta;Q_{02},\omega_{02})\big[1+\exp\big(a_1\eta^2+b_1\eta+c_1\big)\big], \tag{12}$$

$$\Delta L(t_E)\Big/\Big\{L_{\rm crit}\big[M_P/(M_{\rm rg}+M_P)\big]^2\Big\} = \big(1/\tilde{I}\big)\eta^{-4}S_2(\eta,Q_{02},\omega_{02})\big[1+\exp\big(a_2\eta^2+b_2\eta+c_2\big)\big], \tag{13}$$

where M_P is the perturber mass. For the red giant models of various evolutionary stages, the transfer functions are computed with the estimates of ω_{02} and Q_{02} from equations (B9) and (B10) in Appendix B. For the main-sequence stars, the values of ω_{02} and Q_{02} are taken from Lee & Ostriker (1986) for a polytrope of index $N = 1.5$. We may determine the coefficients in these formulae by applying the fitting procedure with the nonlinear least-squares

Marquardt-Levenberg algorithm to our data plotted in Figure 9 for the red giant models of radii 20 and 85 $R_\odot$. The fitting curves are plotted in the figure, which converges into a unique relationship in the nonlinear regime for the red giant models of different radii. The fitting curves for the models with other radii (core masses) are also derived by adopting the same data in the nonlinear regime, as shown for the model of 40 $R_\odot$ in Figure 9. These fitting parameters, thus obtained for the various red giant models, are expressed as the second-order polynomials of radius as

$$
\begin{aligned}
a_1 &= -7.8\times10^{-5}(R_{\rm rg}/R_\odot)^2 + 9.6\times10^{-3}(R_{\rm rg}/R_\odot) - 0.66,\\
b_1 &= 9.0\times10^{-5}(R_{\rm rg}/R_\odot)^2 - 0.028(R_{\rm rg}/R_\odot) + 3.7,\\
c_1 &= -5.4\times10^{-4}(R_{\rm rg}/R_\odot)^2 + 0.077(R_{\rm rg}/R_\odot) - 4.6,\\
a_2 &= -4.6\times10^{-6}(R_{\rm rg}/R_\odot)^2 + 0.00104(R_{\rm rg}/R_\odot) - 0.05945,\\
b_2 &= 2.6\times10^{-4}(R_{\rm rg}/R_\odot)^2 + 0.0127(R_{\rm rg}/R_\odot) + 1.02,\\
c_2 &= 2.2\times10^{-4}(R_{\rm rg}/R_\odot)^2 + 0.036(R_{\rm rg}/R_\odot) - 1.42. \qquad (14)
\end{aligned}
$$

Furthermore, in the nonlinear regime, the deposited energy and angular momentum during the encounters may be given simply as the functions of η in the form

$$
\begin{aligned}
\Delta E(t_E) &= E_{\rm crit}\left[M_P/\left(M_{\rm rg}+M_P\right)\right]^2\\
&\quad\times\exp\left(2.718-0.761\eta-0.386\eta^2\right), \qquad (15)\\
\Delta L(t_E) &= L_{\rm crit}\left[M_P/\left(M_{\rm rg}+M_P\right)\right]^2\\
&\quad\times\exp\left(3.735-2.237\eta-0.040\eta^2\right), \qquad (16)
\end{aligned}
$$

which are plotted in this figure by dashed curves. Note that they coincide with the expressions obtained above in equations (12) and (13) for close encounters of $\eta \lesssim 4$ and $\lesssim$10, respectively. These formulae are applicable not only to the encounter of red giants but also to that of main-sequence stars of arbitrary mass and radius as long as the stellar mass is small enough for the surface convection to develop deep enough to be approximated by a polytrope of index $N = 1.5$.

4.2. *Accreted Mass onto Main-Sequence Stars*

During the encounter, matter near the very surface may gain a lot of energy and angular momentum from the orbital motion to expand and eventually be captured by the perturber. The matter accreted onto the perturber returns the acquisitions back to the orbital motion, which may reduce the transfer of energy and angular momentum at small $\eta < 2$, as stated above. As seen from Table 1, the accreted mass, $M_{\rm acc}(t_E)$, turns out to be nearly the same among the models with similar values of $\Delta E(t_E)/(GM_{\rm rg}^2/R_{\rm rg})$ regardless of the radius of the red giants. This is indicative that the amount of accreted mass is related to the deposited energy. In this section we study the relationship between the accreted mass and other physical quantities and attempt to express the accreted mass as a function of the model parameters.

In the case of a star filling the Roche lobe in a close binary, Paczynski & Sienkiewics (1972) argue that the mass transfer rate is related to the excess, ΔR, of stellar radius over the Roche lobe under the assumption of a polytrope; the principal part of parameter dependences of the transfer rate (see their eq. [A21]) is approximated by

$$
\dot{M} \sim 4\pi A^2\left(\frac{GM}{A}\right)^{N+0.5}\left(\frac{M_{\rm rg}}{M}\right)^{N+1.5}K^{-N}\left(\frac{\Delta R}{R_L}\right)^{N+1.5}, \qquad (17)
$$

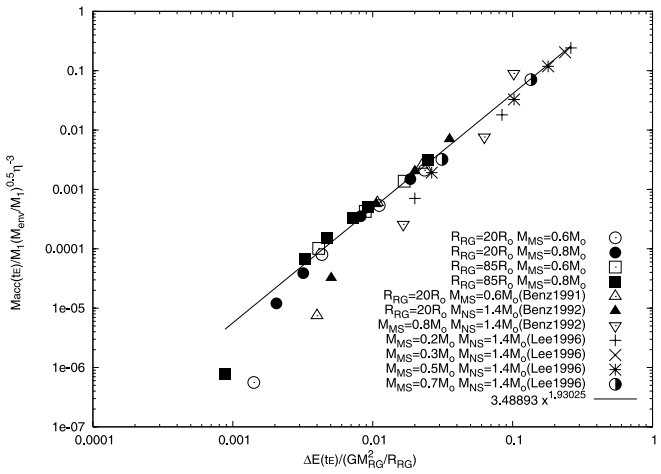

FIG. 10.—Accreted mass, multiplied by the root of the mass fraction of the envelope of the red giant and divided by the third power of the encounter closeness parameter, η, as a function of the energy, $\Delta E(t_E)$, deposited into the red giant envelope. Symbols are the same as in Fig. 9, and solid curve represents a power-law fitting. See text for details.

where A and M are the separation and total mass of the binary system, respectively. Here we neglect the weak dependence on the mass ratio and, in particular, take the Roche radius $R_L/A \approx 0.38$ (cf. eq. [4]). Although the flow is not in the steady state in our case, the timescale of flow through the inner Lagrangian point is slower than the dynamical timescale of the stellar envelope, and hence, we may assume the same dependences for the accreted mass. Further, since the orbit is eccentric and not circular, it is difficult to estimate $\Delta R/R_L$ exactly. And yet, it seems natural for $\Delta R/R_L$ to be related to the deposited energy, and we may well assume the following relation,

$$
\frac{(d\phi_L/dr)\Delta R_L}{GM/R_{\rm rg}} = \frac{\Delta R_L}{R_L}\frac{R_{\rm rg}}{R_L} \sim f\left(\frac{\Delta E}{GM_{\rm rg}^2/R_{\rm rg}}\right), \qquad (18)
$$

where taking account of the work against the gravitational potential (ϕ_L) at the Roche lobe surface and the right most term indicates the left ones will be approximated by a functional form of the deposited energy. By using the relation between the polytropic constant K and the stellar surface characteristics in equation (A7), we then have

$$
\dot{M} \sim M_{\rm rg}\left(\frac{M_{\rm rg}}{M_{\rm env}}\right)^{N-1}\frac{\Omega_{\rm rg}^3}{\Omega_{\rm pass}^2}f\left(\frac{\Delta E}{GM_{\rm rg}^2/R_{\rm rg}}\right)^{N+1.5}, \qquad (19)
$$

where we have replaced the orbital angular velocity by the instantaneous angular velocity, $\Omega_{\rm pass}$ [$=(GM/A^3)^{1/2}$], of the circular orbit at the periastron distance. Consequently, multiplying equation (19) by the periastron passage time $\sim\Omega_{\rm pass}^{-1}$ and putting $N = 1.5$ leads us to

$$
M_{\rm acc} \sim M_{\rm rg}(M_{\rm env}/M_{\rm rg})^{-1/2}\eta^3 f\left(\Delta E/\left(GM_{\rm rg}^2/R_{\rm rg}\right)\right)^3. \qquad (20)
$$

Figure 10 shows the accreted mass, $M_{\rm acc}(t_E)$, divided by $M_{\rm rg}(M_{\rm env}/M_{\rm rg})^{-1/2}\eta^3$, against $\Delta E(t_E)/(GM_{\rm rg}^2/R_{\rm rg})$. It is clearly seen that our numerical results, denoted by open and filled circles and squares, form a unique relationship, indifferent to the mass of the perturber and to the red giant model; a power-law relation is discernible in the range of $\Delta E(t_E) > 3\times10^{-3}GM_{\rm rg}^2/R_{\rm rg}$. For smaller $\Delta E(t_E)$, the accreted mass tends to drop off from the

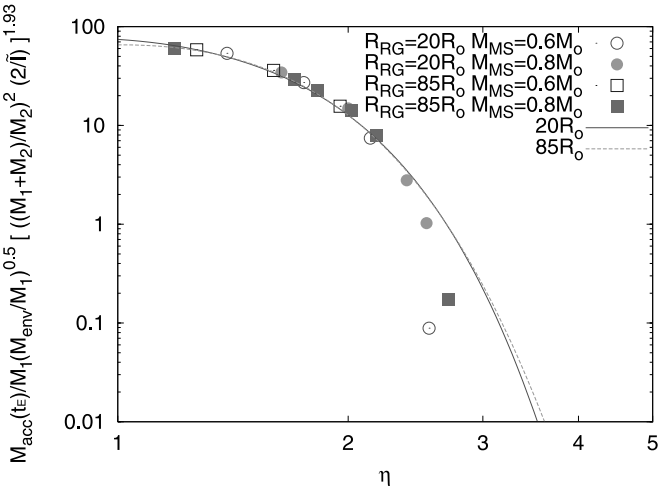

FIG. 11.—Accreted mass, multiplied by $(M_{\rm env}/M_1)^{1/2}(2/\tilde{I}[(M_1M_2)/M_2]^2)^{1.93}$, as a function of η. Symbols are the same as in Fig. 10. Solid and dashed curves are derived from eq. (21) and the fitting formula [eq. (12)] for the red giant models of 20 and 85 $R_\odot$, respectively (see text for details). [*See the electronic edition of the Journal for a color version of this figure.*]

power-law relationship because of the low mass resolution due to the limited number of gas particles; in actuality, only a few gas particles are accreted around $\Delta E(t_E) \sim 3 \times 10^{-3} GM_{\rm rg}^2/R_{\rm rg}$. In Figure 10 we plot the results of the simulations by Davies et al. (1991, 1992) and Lee et al. (1996) and find that their values also fall very closely onto the same relationship for relatively large deposited energy, while the lower mass resolution in these earlier simulations (7500 and 9185 SPH particles, respectively) causes the deviation at smaller $\Delta E(t_E)/GM_{\rm rg}^2/R_{\rm rg}$. If these results for the encounter with main-sequence stars are included, the power relationship holds in the range of mass accretion over 4 orders of magnitude or more.

The power-law fitting to equation (20) yields

$$\frac{M_{\rm acc}}{M_{\rm rg}} = 3.5\left(\frac{M_{\rm env}}{M_{\rm rg}}\right)^{-1/2} \eta^3 \left[\frac{\Delta E(t_E)}{GM_{\rm rg}^2/R_{\rm rg}}\right]^{1.93}, \qquad (21)$$

which gives the accreted mass as a function of the model parameters along with the fitting formula of $\Delta E(t_E)$ from equation (12) or from equation (15). This relation implies that $\Delta R/R_L \propto \Delta E^{1.93/3}$. We show the comparison between this relation and the results of simulations in Figure 11 as a function of η, which is more useful than that of $\Delta E(t_E)$. It shows a good agreement for both the red giant models. Since we may regard the deviations for large η ($\gtrsim$2.5) as due to the low resolution in mass in the simulations, this gives a reasonable fitting for the accreted mass as a function of η for any given set of the model parameters of encounters.

5. CONCLUSIONS AND DISCUSSION

We have performed the SPH simulations of tidal encounters of red giants with environment stars and investigate the characteristics of stellar interactions for a variety of sets of parameters, the evolutionary stages of the red giant, the mass of the perturber stars, and the assumed strength of viscosity, as well as the orbital parameters of the encounter. Based on our results and the other extant models, we discuss the dependences of interactions in the nonlinear regime on the stellar and encounter parameters and propose formulae to describe the energy and angular momentum deposition to red giants and the mass accretion onto the perturber stars in simple and convenient forms as a function of these parameters. Our main quantitative results are as follows.

1. We obtain both the amounts of energy and angular momentum, transferred from the orbital motion into the oscillation and rotation of red giants, during tidal encounters by numerical simulations. The angular momentum deposited in the red giants can be large enough to rotate the envelope at a rate $\Omega \gtrsim 0.01\Omega_{\rm rg}$ for the encounter of periastron distance $r_p/R_{\rm rg} \lesssim 2.5$ (or the impact parameter $b/R_{\rm rg} \lesssim 15.7$) and, hence, for such encounters that ended in the two stars flying apart. For still closer encounters, it increases to give rotation rates significantly exceeding $\Omega \simeq 0.1\Omega_{\rm rg}$. Accordingly, the tidal encounter works as the source of angular momentum necessary to trigger rotational mixing in the red giants and also to explain the origin of fast rotators observed among the HB stars. For the larger radius red giant model and, hence, later stage of evolution, the transferred angular momentum increases while the energy deposition decreases, since the transferred quantities are scaled with the stellar parameters. The fitting formulae are derived to describe these quantities as a function of the mass and radius of red giants, subject to the perturbation, the mass of the main-sequence stars as a perturber, and the impact parameter. Furthermore, we show that these transferred quantities, when normalized with respect to the momentum of inertia of the models, are given solely as functions of the encounter closeness parameter η. Our fitting formulae agree well with the results of encounter simulations by other authors and can even reproduce the results for the encounters of main-sequence stars approximated to a polytrope of index $N = 1.5$.

2. With the aid of fine mass resolution, we demonstrate that the main-sequence stars can capture gas from the red giant envelope sufficiently to disguise their surface with accreted matter even for the encounters that ended in a flyby with an evolved red giant. The accreted mass onto the main-sequence star as a perturber during the tidal encounters is shown to be in a direct relationship with the energy deposition into the red giants. We also derive the formula which predicts the accreted mass as a function of the impact parameters for given stellar parameters and is applicable to the encounters involving not only the red giants but also the main-sequence stars.

The derived formulae are useful in determining the periastron distance of the tidal capture limit for the encounters with various model parameters. They can also be useful for inquiring whether some stellar objects in the globular clusters, for example, the red giants and the main-sequence stars with abundance anomalies and the fast rotating HB stars, which cannot be explained through the framework of the normal stellar evolution, can be produced through the stellar interactions. In our computations, the mass accretion rate may exceed the Eddington limit ($\dot{M}_{\rm Edd} = 4\pi cR_{\rm ms}/\kappa_e$) on the surface of the main-sequence star for very close encounters, but since it remains below the Eddington limit at the accretion radius, we may well assume that the accreted mass mostly settles on the surface of the main-sequence stars with loosing thermal energy. In the following, we discuss the application of these formulae and the possibility that such stellar objects have their origins in the stellar encounters.

5.1. *Tidal Capture Limit and Comparisons with Other Works*

In our simulations, the tidal capture limits, $r_{p,\rm cap}$ in periastron distance and $\eta_{\rm cap}$ in η, are estimated from the condition that $\Delta E(t_E) = (1/2)\mu v_\infty (10\ {\rm km\ s})^2$ with the use of equation (12) or equation (15). Our estimates are given in Table 2 for the two red

giant models with the perturber masses of 0.6, 0.8, and 1.4 $M_\odot$. For the red giant of larger radius, the tidal capture limits decrease slightly ($\sim$10%) when normalized with respect to the radius of the red giant, but increase in the physical dimensions nearly in proportion to the surface radius; they slightly increase with the mass of the perturber. For the encounter of a $M_{\rm rg} = 0.8\ M_\odot$ red giant with a $M_{\rm ms} = 0.6\ M_\odot$ main-sequence star, Davies et al. (1991, 1992) give the periastron distances for the tidal capture limit in the range of $2.00 < r_{p,{\rm cap}}/R_{\rm rg} < 2.25$, and our estimate, $r_{p,{\rm cap}}/R_{\rm rg} = 2.1$, as seen from Table 2, resides in their range. On the other hand, our estimates turn out to be larger by $\sim$20% than those obtained from the linear analysis by McMillan et al. (1990) as listed in the table.

On the other hand, Khokhlov et al. (1993a, 1993b) compute the encounter of a polytrope star of mass $M_* = 0.8\ M_\odot$ with a black hole of mass $M_B \gg M_*$ for various values of the polytropic index (the relative velocity is 100 km s^{-1} at infinity). The tidal capture limit decreases from $\eta_{\rm cap} = 2.75$ for $N = 1.5$ to 2.20 and 1.55 for $N = 2.0$ and 3.0, respectively. This demonstrates that for larger polytrope index, the energy deposition rate of the star becomes smaller because of the increase in the mass concentration toward the center and because of the decrease in the moment of inertia for a given mass and radius.

5.2. *Relevance to the Origin of Stars with Anomalous Abundances in Globular Clusters*

We may apply our fitting formulae to examine the possibility that the abundance anomalies observed for both red giants and main-sequence stars in some globular clusters can be explained in terms of the stellar interactions during the close encounters. As the origin of these objects, we propose the following scenario. (1) The anomalies of red giants are generated through the flash-assisted deep mixing mechanism that is triggered by the injection of angular momentum into their envelope during the encounter with environment stars (Fujimoto et al. 1999). (2) The main-sequence stars gain the abundance anomalies as a result of the surface pollution by accreting matter from the red giants which have already developed these anomalies. We evaluate whether these work under the conditions prevailing in globular clusters.

As for point 1, Fujimoto et al. (1999) argue that the angular momentum of $\Delta L_{\rm rg}/L_{\rm crit} \gtrsim 1/100$ is necessary to induce the flash-assisted deep mixing, and the transfer of angular momentum of this order occurs during the encounter of $\eta \lesssim 3$, and hence, $r_p \sim 2.6 R_{\rm rg}$ from our formulae. The transfer of angular momentum may have relevance to the bimodal distribution of rotation velocity that HB stars display with the fastest rotators distributed on the cooler (redder) side of the branch, whereas the slower rotators spread over a wider range on the branch. Suda & Fujimoto (2006) suggest that the different modes of the helium-mixing mechanism may result according to when the stars undergo the close encounter and the deposition of angular momentum on the RGB and influence the HB morphology; the injection of angular momentum may invoke hydrodynamical instabilities due to differential rotation and invoke turbulent mixing to trigger the hydrogen-flash-driven deep mixing, and the resultant helium enrichment in the envelope accelerates the evolution of RGB. The stars that experience the helium enrichment at an earlier epoch on the RGB have a smaller mass of the helium core and, hence, are located on the redder side of the HB and those with a later mixing epoch shift to blueward; on the other hand, if the stars experience the close encounter near the tip of the RGB, the helium-flash-driven mixing, rather than the hydrogen-flash-driven deep mixing, takes places and causes the largest decrease of the helium core so that the stars are situated at the reddest end on the HB. If the stars experience a close encounter at an earlier stage of the RGB, then they become slow rotators due to angular momentum loss through mass loss on the RGB and, hence, settle on the redder side of the HB, and the stars, if experiencing it at a later stage of the RGB, become faster rotators and settle on the bluer side. Finally, the stars, which undergo close encounters very close to the tip of the RGB, become the fastest HB rotators, located on the redmost side of the branch. The close encounters at $\eta \lesssim 3$ can explain the fastest rotation rates observed from HB stars of $\Omega \sim 0.1\Omega_{\rm K}$ if the angular momentum is conserved during the contraction from the RGB to the HB. While the pristine angular momentum is effectively lost for such low-mass stars, such fast rotation as observed for HB stars may be expected also from the synchronization of red giants in binary systems of separation (more than several AU), and yet, it is difficult for such binaries to survive without suffering encounters in the dense stellar environment of globular clusters (see below eq. [22]). In other words, we may take the existence of HB stars of these fastest rotations as evidence that such close encounters as $\eta \lesssim 3$ take place in these clusters.

As for point 2, since the mass in the surface convective zone is of $\sim 3 \times 10^{-3}\ M_\odot$, the accreted mass of the order of $\sim 10^{-3}\ M_\odot$ suffices to disguise the surface abundances with those transferred from the red giant envelope with anomalous abundances. From the present results, it is possible to estimate the range of periastron distance, η, that can allow the accreted mass of this order at $\eta = 1.8$–2.2 and 1.5–2.0, which correspond to $r_p = 1.9 R_{\rm rg}$–$2.1 R_{\rm rg}$ and $1.7 R_{\rm rg}$–$2.0 R_{\rm rg}$, for $R_{\rm rg} = 20$ and 85 $R_\odot$, respectively, for masses of the main-sequence stars of 0.6 and 0.8 $M_\odot$.

The timescale of tidal interactions in the environment where the stellar density is n_f pc^{-3} and the velocity dispersion v_∞, is estimated (with the gravitational focusing taken into account, because of low velocity dispersion of environment stars in the core) at

$$\tau_{\rm enc} \sim 7.4 \times 10^9 \frac{10^4\ {\rm pc}^{-3}}{n_f} \frac{100\ R_\odot}{r_p} \times \frac{v_\infty}{10\ {\rm km\ s}^{-1}} \left(\frac{M_1 + M_2}{2\ M_\odot} \right)^{-1} {\rm yr}. \quad (22)$$

On this basis, the timescales of tidal encounters, which can bring about a mass accretion of the order of $10^{-3}\ M_\odot$ and an angular momentum transfer of $\Delta L_{\rm rg}/L_{\rm crit} \gtrsim 1/100$, are estimated at $\sim 1.5 \times 10^{10}$ yr for 20 $R_\odot$ and $\sim 3 \times 10^9$ yr for 85 $R_\odot$ in the environment of $n_f = 10^4$ pc^{-3} and $v_\infty = 10$ km s^{-1}. If the tidal interactions are responsible for these observed objects, then these timescales are too large to explain the objects by tidal interactions as compared with the lifetimes on the corresponding stages of red giants, $\sim 10^8$ yr for 20 $R_\odot$ and $\sim 10^7$ yr for 85 $R_\odot$, and the accumulated number of close encounters, attendant with the abundance anomalies, seems to be no more than a few, too small to explain the observations even in rough estimates. In order for the encounters to be viable, these timescales have to be shorter by more than an order of magnitude, and accordingly, there needs to be some mechanism(s) to enhance the frequency of tidal encounters in globular clusters.

Sugimoto (1996) points out the importance of mass segregation in modeling dynamical evolution of star clusters to explain the observable number of millisecond pulsars in 47 Tuc; without the mass segregation, theoretical estimation indicates that the formation probability of a binary with a neutron star is higher in ω Cen, which has no collapsed core, than 47 Tuc, which has

a collapsed core, although in actuality, the former has not been reported to contain any pulsars. Moreover, mass segregation promotes the core collapse and makes it happen more rapidly than in the case of a single-mass component. Portegies Zwart et al. (2001) confirm that mass segregation enriches the core of a star cluster in giants and white dwarfs by *N*-body simulations for an open star cluster. In order to explain the observable number of giants with abundance anomalies, about a half of the total number of giants have to experience tidal encounters with field stars. It is necessary to see whether the mass segregation can gather most of the giants, although not all, in the core and can increase the two-body encounter rate by more than an order of magnitude. In addition to the mass segregation, the gravothermal oscillations of star clusters, which has been proposed by Bettwieser & Sugimoto (1984) and confirmed by *N*-body simulation (Makino 1996), may influence the rate; since the interactions are expected to occur in the evolutional stage near the high-density peak, it is necessary to investigate in a correct manner how deeply and how long such a high-density state must reach and last to affect the encounter rates.

For the encounter with the red giants of later stages, the pollution of main-sequence stars is possible even when the two stars fly apart after the encounters. For the encounter that ends in the formation of a binary, it depends on the fate of the two stars whether the abundance anomalies imprinted onto the companions are observable or not, and it is necessary to pursue the details of evolution of tidally captured binaries. There are many effects that influence the binary evolution, such as the spin-up and mode damping rates of the red giant after the encounter, the mass transfer to the companion at subsequent periastron passages (e.g., Sepinsky et al. 2007), the mass loss from the bound system, and also the expansion of the red giant as it ascends the RGB. In addition, we should also take into account the tidal interactions of formed binaries with the environment stars. We may conceive that the destination of a tidally captured binary is either one component is liberated through the exchange encounter with a third body or the two stars eventually coalesce as a result of Roche lobe overflow. The possibility of the exchange event depends on the evolution timescale of giants and the encounter timescale; since the exchange encounter rate is proportional nearly to the semimajor axis of a binary under the assumption of the point mass limit (Heggie et al. 1996), the former is expected to occur more frequently. Accordingly, if tidal capture of two-body encounters can contribute the modification of stellar populations, then the exchange encounters follow at larger rates and make greater contributions. This increase in the encounter rates with the red giant in the binary may affect the statistics of main-sequence stars with abundance anomalies. Furthermore, through the exchange encounters, the red giants and HB stars, now losing mass due to the mass loss and becoming lighter than the heaviest main-sequence stars, can be ejected from the binary systems to fly apart as single stars.

In summary, the enhancement of tidal interactions, necessary to explain the observed abundance anomalies, is expected to be provided by the formation of a high-density core due to the gravothermal oscillations and by the mass segregations which enlarge the fractions of stars from the upper mass end in the core. A proper understanding of these effects waits for *N*-body simulations of globular clusters with the stars of multiple mass spectra taken into account, since star-star interactions as studied in the present work will play a critical role. In these studies of dynamical evolution of stellar systems, the formulae for the transfer of energy, angular momentum, and accreted mass derived in the present work serve the purpose of incorporating these effects into the simulations. It is also necessary to pursue the binary evolution and accurately explore the fate of red giants and subsequent HB stars with the interactions with the environment stars taken into account.

This paper is based on one of the author's (S. Y.) dissertation submitted to Hokkaido University, in partial fulfillment of the requirement for the doctorate. This work has been partially supported by Grants-in-Aid for Scientific Research (15204010, 16540213, and 18104003) from the Japan Society for the Promotion of Science.

APPENDIX A

THE POLYTROPE MODEL OF RED GIANT STRUCTURE

Fujimoto & Tomisaka (1992) show that the structure of a red giant can be modeled by a combination of two polytropes with the cool and hot components corresponding to the core and envelope, respectively. In particular, we may replace the cool component as a sphere of uniform density (i.e., a polytrope of index $N = \infty$), since we are interested only in the envelope structure, and in this case, the structure of hot components ensues from the following equations,

$$\frac{dM_r}{dr} = 4\pi r^2 \rho, \tag{A1}$$

$$\frac{1}{\rho}\frac{dP}{dr} = -\frac{GM_r}{r^2} + g, \tag{A2}$$

with the contribution of core gravity, g, in equation (3) taken into account. With a given envelope mass, $M_{\rm env}$, and the surface radius, R, we may introduce the dimensionless variables as

$$M_r = M_{\rm env}\varphi, \qquad r = R\xi, \qquad \rho = \rho_0\theta^N, \qquad P = P_0\theta^{N+1}, \tag{A3}$$

where ρ_0 and P_0 are the density and pressure coefficients, related to the envelope mass and radius as

$$\rho_0 = M_{\rm env}/4\pi R^3, \qquad P_0 = GM_{\rm env}^2/4\pi(N+1)R^4. \tag{A4}$$

By using these variables, we may rewrite the equations in the nondimensional form, corresponding to the Lane-Emden equation, as

$$\frac{1}{\xi^2}\frac{d}{d\xi}\left(\xi^2\frac{d\theta}{d\xi}\right) = \begin{cases} -\theta^N - 3\varphi_{\rm core}/\xi_{\rm core}^3, & \xi < \xi_{\rm core}, \\ -\theta^N, & \xi \geq \xi_{\rm core}, \end{cases} \tag{A5}$$

where $\xi_{\rm core} = R_{\rm core}/R$ and $\varphi_{\rm core} = M_{\rm core}/M_{\rm env}$. In the above equations, we take into account the hot component in the core, but its contribution to the envelope mass is negligible because of a small core radius.

We may obtain the envelope structure of red giants by solving equation (A5) for a given set of core radius and mass ($\xi_{\rm core}, \varphi_{\rm core}$) with the boundary conditions

$$d\theta/d\xi = 0, \quad \varphi = 0 \quad \text{at } \xi = 0; \qquad \theta = 0, \quad \varphi = 1 \quad \text{at } \xi = 1. \tag{A6}$$

Several solutions are shown in Figure 1, and we see that the structures exterior to the core resemble each other as long as the core radius is sufficiently smaller than the stellar radius ($\xi_{\rm core} \ll 1$) and unless the envelope mass is much smaller or much larger than the core mass. In particular, we have a relation between the polytropic constant (or entropy) and the surface characteristics of the red giant analogous to the single polytrope,

$$K = \frac{P_0}{\rho_0^{1+1/N}} = \frac{(4\pi)^{1/N}G}{N} M_{\rm env}^{1-1/N} R^{3/N-1}. \tag{A7}$$

APPENDIX B

MODEL DEPENDENCES OF TRANSFER OF ENERGY AND ANGULAR MOMENTUM DUE TO LINEAR DYNAMICAL TIDE

The linear perturbation theory of dynamical tides has been developed to estimate the deposition of energy and angular momentum from the orbital motion to the stellar oscillations. Press & Teukolsky (1977) derive an analytic formula for the energy deposition, and later, Lai (1997) extends it with the stellar rotation taken into account to give the general formulae for both the energy deposition and angular momentum transfer, which are applicable for $\eta \gg 1$. We are here concerned with the red giants that have negligible rotation initially. Furthermore, we may well retain only a leading term of $l = 2$ f-modes, which dominate the dynamical tides (see Lee & Ostriker 1986).

Press & Teukolsky (1977) give the energy loss, ΔE, of the orbital motion into the adiabatic, nonradial oscillations for a star of mass, M_1, and radius, R_1, during an encounter of periastron distance r_p with a point object of mass M_2, in the following formula,

$$\Delta E = \frac{GM_1^2}{R_1}\left(\frac{M_2}{M_1}\right)^2 \sum_{l=2,3,\ldots} \left(\frac{R_1}{r_p}\right)^{2l+2} T_l(\eta), \tag{B1}$$

where the dimensionless transfer function, T_l, is defined by

$$T_l(\eta) = 2\pi^2 \sum_n |Q_{nl}|^2 \sum_{m=-l}^{l} |K_{nlm}|^2 \tag{B2}$$

with the overlap integral, Q_{nl}, given by

$$Q_{nl} = \int_0^{R_1} r^2\, dr\, \rho l (r/R_1)^{l-1} \left[\xi_{nl}^R(l)\xi_{nl}^S\right], \tag{B3}$$

and with the integral, K_{nlm}, along the trajectory given by

$$K_{nlm} = \frac{W_{lm}}{2\pi} 2^{3/2} \eta I_{lm}(\eta\omega_{nl}), \tag{B4}$$

$$I_{lm}(y) = \int_0^\infty dx \left(1 + x^2\right)^{-l} \cos\left[2^{1/2} y\left(x + x^3/3\right) + 2m \tan^{-1} x\right], \tag{B5}$$

$$W_{lm} = (-)^{(l+m)/2} \left[\frac{4\pi}{2l+1}(l-m)!(l+m)!\right]^{1/2} \Big/ \left[2^l \left(\frac{l-m}{2}\right)! \left(\frac{l+m}{2}\right)!\right]. \tag{B6}$$

Here ξ_{nl}^R and ξ_{nl}^S are the radial and poloidal normal mode components of the Lagrangian displacements from the unperturbed spherically symmetric state in units of $M_1^{-1/2}$, respectively, and the symbol $(-)^k$ in equation (B6) is to be interpreted as $(-1)^k$ when k is an integer and zero when k is not an integer. Since $T_l(\eta)$ includes the stellar mode frequency, ω_{nl}, and the overlap integrals, Q_{nl}, both determined from the normal mode structures, $\Delta\tilde{E}$ is dependent on the mode oscillation structure of the star.

For the leading term of the $l = 2$ f-mode, we have the following form by separating the dependences on the mass and radius of stars as

$$\Delta E_2 = \left(GM_1^2/R_1\right)(M_2/M_1 + M_2)^2 \eta^{-4} T_2(\eta; Q_{02}, \omega_{02}), \tag{B7}$$

$$T_2(\eta; Q_{02}, \omega_{02}) = \frac{4\pi}{5} |Q_{02}|^2 \left\{ I_{20}(\eta\omega_{02})^2 + \frac{3}{2}\left[I_{22}(\eta\omega_{02})^2 + I_{2-2}(\eta\omega_{02})^2\right] \right\}. \tag{B8}$$

For the red giants of $M_1 = M_{\rm rg} = 0.8\ M_\odot$, the frequency, ω_{02}, and the overlap integral, Q_{02}, of $l = 2$, f-mode oscillations are obtained by McMillan et al. (1990) who solve the perturbation equations to find the overlap integral and stellar mode frequency. We may evaluate the values of ω_{02} and Q_{02} by interpolating their results as a function of the radius in the following forms,

$$\omega_{02} = -1.56 \times 10^{-4}(R_{\rm rg}/R_\odot)^2 + 0.0112(R_{\rm rg}/R_\odot) + 1.84, \tag{B9}$$

$$Q_{02} = 2.29 \times 10^{-5}(R_{\rm rg}/R_\odot)^2 - 0.00352(R_{\rm rg}/R_\odot) + 0.331. \tag{B10}$$

As for the angular momentum, ΔL, transferred from the orbit to the spin of the primary star, Lai (1997) derives a general form with the effects of stellar rotation taken into account. In the limit of negligible initial rotation rate, it reduces to

$$\Delta L = \left(GM_1^3 R_1\right)^{1/2} \left(\frac{M_2}{M_1}\right)^2 \sum_{l=2,3,\ldots} \left(\frac{R_1}{r_p}\right)^{2l+2} S_l(\eta), \tag{B11}$$

where the transfer function, S_l, is defined as

$$S_l(\eta) = -2\pi^2 \sum_n |Q_{nl}|^2 \omega_{nl}^{-1} \sum_{m=-l}^{l} m |K_{nlm}|^2 \tag{B12}$$

with the overlap integral, Q_{nl}, and the trajectory integral, K_{nlm}, defined above.

Then for the $l = 2$ f-mode, we have

$$\Delta L_2 = \sqrt{GM_1^3 R_1} \left(\frac{M_2}{M_1 + M_2}\right)^2 \eta^{-4} S_2(\eta; Q_{02}, \omega_{02}), \tag{B13}$$

where

$$S_2(\eta; Q_{02}, \omega_{02}) = -\left(\frac{12\pi}{5}\right) |Q_{02}| \omega_{02}^{-1} \left[I_{22}(\eta\omega_{02})^2 - I_{2-2}(\eta\omega_{02})^2\right]. \tag{B14}$$

REFERENCES

Aikawa, M., Fujimoto, M, Y., & Kato, K. 2001, ApJ, 560, 937
———. 2004, ApJ, 608, 983
Bailyn, B. C. 1988, Nature, 332, 330
———. 1995, ARA&A, 33, 133
Bate, M. R., Bonnell, I. A., & Price, N. M. 1997, MNRAS, 285, 33
Beccari, G., Ferraro, F. R., Possenti, A., Valenti, E., Origlia, L., & Rood, R. T. 2006, AJ, 131, 2551
Bedin, L. R., Piotto, G., Anderson, J., Cassisi, S., King, I. R., Momany, Y., & Carraro, G. 2004, ApJ, 605, L125
Beer, M. E., & Davies, M. B. 2004, MNRAS, 348, 679
Behr, B. B., Cohen, J. G., & McCarthy, J. K. 2000a, ApJ, 531, L37
Behr, B. B., Djorgovski, S. G., Cohen, J. G., McCarthy, J. K., Côtè, P., Piotto, G., & Zoccali, M. 2000, ApJ, 528, 849
Benz, W. 1990, in The Numerical Modeling of Nonlinear Stellar Pulsations: Problems and Prospects, ed. J. R. Buchler (Dordrecht: Kluwer), 269
Benz, W., Bower, R. L., Cameron, A. G. W., & Press, W. 1990, ApJ, 348, 647
Bettwieser, E., & Sugimoto, D. 1984, MNRAS, 208, 493
Briley, M. M., Smith, G. H., Bell, R. A., Oke, J. B., & Hesser, J. E. 1992, ApJ, 387, 612
Cannon, R. D., Croke, B. F. W., Bell. R. A., Hesser, J. E., & Stathakis, R. A. 1998, MNRAS, 298, 601
Cohen, J. G. 1999, AJ, 117, 2434
Cohen, J. G., & McCarthy, J. K. 1997, AJ, 113, 1353
Da Costa, G. S. 1997, in IAU Symp. 189, Fundamental Stellar Properties: The Interaction between Observation & Theory, ed. T. R. Bedding, A. J. Booth, & J. Davis (Dordrecht: Kluwer), 193
D'Antona, F. 2004, Mem. Soc. Astron. Italiana, 75, 388
D'Antona, F., & Caloi, V. 2004, ApJ, 611, 871
Davies, M. B. 1995, MNRAS, 276, 887
Davies, M. B., Benz, W., & Hills, J. G. 1991, ApJ, 381, 449
———. 1992, ApJ, 401, 246
Djorgoski, S., Piotto, G., Phinney, E. S., & Chernoff, D. F. 1991, ApJ, 372, L41
Faber, J. A., Rasio, F. A., & Willems, B. 2005, Icarus, 175, 248
Fabian, A. C., Pringle, J. E., & Rees, M. J. 1975, MNRAS, 172, P15
Fenner, Y., Campbel, S., Karakas, A. I., Lattanzio, J. C., & Gibson, B. K. 2004, MNRAS, 353, 789
Ferraro, F. R. 2006, preprint (astro-ph/0601217)
Ferraro, F. R., Beccari, G., Rood, R. T., Bellazzini, M., Sills, A., & Sabbi, E. 2004, ApJ, 603, 127
Ferraro, F. R., Paltrinieri, B., Rood, R. T., & Dorman, B. 1999, ApJ, 522, 983
Ferraro, F. R., Sills, A., Rood, R. T., Paltrinieri, B., & Buonanno, R. 2003, ApJ, 588, 464
Ferraro, F. R., et al. 1997, A&A, 324, 915
Fujimoto, M. Y., Aikawa, M., & Kato, K. 1999, ApJ, 519, 733
Fujimoto, M. Y., Sugiyama, K., Iben, I., Jr., & Hollowel, D. 1995, ApJ, 444, 175
Fujimoto, M. Y., & Tomisaka, K. 1992, ApJ, 385, 445
Gratton, R. G., et al. 2001, A&A, 369, 87
Heggie, D. C., Hut, P., & McMillan, S. L. W. 1996, ApJ, 467, 359
Hills, J. G. 1976, MNRAS, 175, P1
Hills, J. G., & Day, C. A. 1976, Astrophys. Lett., 17, 87
Hut, P., et al. 2003, NewA, 8, 337
Ivanov, P. B., & Papaloizou, C. B. 2004, MNRAS, 347, 437
James, G., et al. 2004, A&A, 414, 1071
Khokhlov, A., Novikov, I. D., & Pethick, C. J. 1993a, ApJ, 418, 163
———. 1993b, ApJ, 418, 181
Kraft, R. P. 1994, PASP, 106, 553
Lai, D. 1997, ApJ, 490, 847
Lai, D., Rasio, F. A., & Shapiro, S. L. 1993, ApJ, 412, 593

Lee, H. M., Kim, S. S., & Kang, H. 1996, J. Korean Astron. Soc., 29, 19
Lee, H. M., & Ostriker, J. P. 1986, ApJ, 310, 176
Leigh, N., Sills, A., & Knigge, C. 2007, ApJ, 661, 210
Leonard, P. J. T. 1989, AJ, 98, 217
Lombardi, J. C., Proulx, Z. F., Dooley, K. L., Theriault, E. M., Ivanova, N., & Rasio, F. A. 2006, ApJ, 640, 441
Lombardi, J. C., Warren, J. S., Rasio, F. A., Sills, A., & Warren, A. R. 2002, ApJ, 568, 939
Makino, J. 1996, ApJ, 471, 796
Mapelli, M., Sigurdsson, S., Ferraro, F. R., Colpi, M., Possenti, A., & Lanzoni, B. 2006, MNRAS, 373, 361
McMillan, S. L. W., McDermott, P. N., & Taam, R. E. 1987, ApJ, 318, 261
McMillan, S. L. W., Taam, E. T., & McDermott, P. N. 1990, ApJ, 354, 190
Meglicki, Z., Wickramasinghe, D., & Bicknell, G. V. 1993, MNRAS, 264, 691
Monaghan J, J., & Gingold, R. A. 1983, J. Comput. Phys., 52, 374
Okazaki, A. T., Bate, M. R., Ogilvie, G. I., & Pringle, J. E. 2002, MNRAS, 337, 967
Paczynski, B. 1971, ARA&A, 9, 183
Paczynski, B., & Sienkiewics, R. 1972, Acta Astron., 22, 73
Paltrinieri, B., Ferraro, F. R., Paresce, F., & de Marchi, G. 2001, AJ, 121, 3114
Peterson, R. C. 1983, ApJ, 275, 737
Peterson, R. C., Rood, R. T., & Crocker, D. A. 1995, ApJ, 453, 214
Piotto, G., et al. 2007, ApJ, 661, L53
Pooley, D., & Hut, P. 2006, ApJ, 646, L143
Pooley, D., et al. 2003, ApJ, 591, L131
Portegies Zwart, S. F., McMillan, S. L. W., Hut, P., & Makino, J. 2001, MNRAS, 321, 199
Press, W. H. 1986, in Use of Supercomputers in Stellar Dynamics, ed. P. Hut & S. L. McMillan (Berlin: Springer), 184
Press, W. H., & Teukolsky, S. A. 1977, ApJ, 213, 183
Rasio, F. A., & Shapiro, S. L. 1991, ApJ, 377, 559
Recio-Blanco, A., Piotto, G., Aparicio, A., & Renzini, A. 2002, ApJ, 572, L71
Sabbi, E., Ferraro, F. R., Sills, A., & Rood, R. T. 2004, ApJ, 617, 1296
Sepinsky, J. F., Willems, B., Kalogera, V., & Rasio, F. A. 2007, ApJ, 667, 1170
Shimada, M., Fujimoto, M. Y., Yamada, S., & Sugimoto, D. 2003, in IAU Symp. 208, Astrophysical Supercomputing using Particle Simulations, ed. J. Makino & P. Hut (San Francisco: ASP), 445
Sneden, C., Kraft, R. P., Guhathakurta, P., Peterson, R. C., & Fulbright, J. P. 2004, AJ, 127, 2162
Suda, T., & Fujimoto, M. Y. 2006, ApJ, 643, 897
Suda, T., Tsujimoto, T., Shigeyama, T., & Fujimoto, M. Y. 2007, ApJ, 671, L129
Sugimoto, D. 1996, in IAU Symp. 174, Dynamical Evolution of Star Clusters, ed. P. Hut & J. Makino (Dordrecht: Kluwer), 1
Suntzeff, N. B., & Smith, V. V. 1991, ApJ, 381, 160
Thoul, A., Jorissen, A., Goriely, S. Jehin, E., Magain, P., Noels, A., & Parmentier, G. 2002, A&A, 383, 491
Ventura, P., D'Antona, F., Mazzitelli, I., & Gratton, R. 2001, ApJ, 550, L65
Warren, S. R., Sandquist, E. L., & Bolte, M. 2006, ApJ, 648, 1026